J. Fluid Mech. (2017), *vol.* 828, *pp.* 496–526.
doi:10.1017/jfm.2017.519

Assessment of suboptimal control for turbulent skin friction reduction via resolvent analysis

Satoshi Nakashima[1], **Koji Fukagata**[1,†] **and Mitul Luhar**[2]

[1]Department of Mechanical Engineering, Keio University, Yokohama 223-8522, Japan

[2]Department of Aerospace and Mechanical Engineering, University of Southern California, Los Angeles, CA 90089, USA

(Received 15 February 2017; revised 5 June 2017; accepted 25 July 2017; first published online 4 September 2017)

This paper extends the resolvent analysis of McKeon & Sharma (*J. Fluid Mech.*, vol. 658, 2010, pp. 336–382) to elucidate the drag reduction mechanisms for the suboptimal control laws proposed by Lee, Kim & Choi (*J. Fluid Mech.*, vol. 358, 1998, pp. 245–258). Under the resolvent formulation, the turbulent velocity field is expressed as a linear superposition of propagating modes identified via a gain-based decomposition of the Navier–Stokes equations. This decomposition enables targeted analyses of the effects of suboptimal control on high-gain modes that serve as useful low-order models for dynamically important coherent structures such as the near-wall (NW) cycle or very-large-scale motions. The control laws generate blowing and suction at the wall that is proportional to the fluctuating streamwise (Case ST) or spanwise (Case SP) wall shear stress, with the magnitude of blowing and suction being a design parameter. It is shown that both Case ST and SP can suppress resolvent modes resembling the NW cycle. However, for Case ST, the analysis reveals that control leads to substantial amplification of flow structures that are long in the spanwise direction. Quantitative comparisons show that these predictions are broadly consistent with results obtained in previous direct numerical simulations. Further, the predicted changes in mode structure suggest that suboptimal control can be considered a modified version of opposition control. In addition to the study of modes resembling the NW cycle, this paper also considers modes of varying speed and wavelength to provide insight into the effects of suboptimal control across spectral space.

Key words: drag reduction, flow control, turbulent flows

1. Introduction

In recent years, many attempts have been made to control fluid flows in order to reduce drag and improve energy efficiency. In the absence of wave drag, the total drag consists of pressure drag and skin friction. To reduce the pressure drag, extensive shape optimization has been performed. This can be seen, for instance, in the historical evolution of the nose shape of bullet trains. In contrast, there are few practical control techniques to reduce skin friction. One notable exception is the polymer injection technique used in the Trans Alaska Pipeline System. While polymer

†Email address for correspondence: fukagata@mech.keio.ac.jp

injection has been successful for internal flows with liquids, there are few practical friction reduction techniques for external air flows. This fundamental limitation is especially important given the fact that skin friction contributes significantly to total drag ($\geqslant 50\,\%$) for commercial aircraft (Gad-el-Hak 1994, 2000). As a result, skin friction reduction has been, and continues to be, the subject of extensive research (Kim 2003; Kasagi, Suzuki & Fukagata 2009; Abdulbari *et al.* 2013).

Skin friction reduction techniques can be broadly classified into active control, which requires energy input for actuation, and passive control, which involves the use of textured surfaces such as riblets (e.g. Walsh & Weinstein 1979). Active control can be further classified into predetermined control and feedback control, depending on whether the actuation is based on real-time sensor information or determined *a priori*. Examples of predetermined control include wall oscillation as reviewed, e.g. by Karniadakis & Choi (2003) and Quadrio (2011), travelling-wave-like blowing and suction (Min *et al.* 2006; Lieu, Moarref & Jovanović 2010; Mamori, Fukagata & Hoepffner 2010; Moarref & Jovanović 2010; Mamori, Iwamoto & Murata 2014) and travelling-wave-like wall deformation (Hoepffner & Fukagata 2009; Nakanishi, Mamori & Fukagata 2012; Tomiyama & Fukagata 2013). Extensive studies have been conducted on the efficacy and drag reduction mechanisms of these predetermined control techniques. For further detail, readers are referred to the references provided above.

1.1. *Feedback control for drag reduction*

Feedback flow controls have also been studied extensively in the past twenty years. The simplest feedback control scheme is the opposition control technique proposed by Choi, Moin & Kim (1994), in which blowing and suction are generated at the wall to counteract the wall-normal velocity component detected at a virtual detection plane above the wall. Choi *et al.* (1994) achieved approximately $25\,\%$ drag reduction using opposition control in their direct numerical simulation (DNS) of low Reynolds number turbulent channel flow. The performance of opposition control has been studied using DNS under a range of different conditions, e.g. at moderate Reynolds numbers (Iwamoto, Suzuki & Kasagi 2002) for various blowing and suction amplitudes (Chung & Talha 2011) and in pipe flow (Fukagata & Kasagi 2003). Motivated by the simulation results above, experimental attempts at feedback control have also been made (Kasagi *et al.* 2009). For instance, Yoshino, Suzuki & Kasagi (2008) constructed an experimental feedback control system, in which local wall deformations were generated to suppress streamwise vortices based on the streamwise wall shear stress signal. This technique succeeded in reducing drag by $6 \pm 3\,\%$ after taking measurement uncertainty into account.

Although conceptually simple, opposition control is very difficult to put into practice because it requires sensors located above the wall. To overcome this problem, Lee, Kim & Choi (1998) proposed theoretical control laws based on suboptimal control theory, which require information measurable at the wall alone, i.e. the wall pressure, the spanwise wall shear stress or the streamwise wall shear stress. DNS conducted by Lee *et al.* (1998) showed a $16\,\%$–$22\,\%$ drag reduction when the wall pressure or the spanwise shear stress were used as the input signal or control objective. However, drag increased when the streamwise wall shear stress was used. Iwamoto *et al.* (2002) confirmed the results obtained by Lee *et al.* (1998), and found that the efficacy of control deteriorates slightly as the Reynolds number increases. Fukagata & Kasagi (2004) extended these suboptimal control techniques by setting a cost function based

on the near-wall Reynolds shear stress, which is directly related to the friction drag (Fukagata, Iwamoto & Kasagi 2002), and succeeded in reducing drag using only the streamwise wall shear stress as a sensor input. We will introduce the details of these suboptimal control laws in § 2.2.

1.2. *Coherent structures in wall turbulence*

Many of the active control techniques mentioned above target the suppression of coherent structures known to be dynamically and energetically important in wall-bounded turbulent flows. Since the pioneering experimental work by Kline *et al.* (1967) and DNS by Kim, Moin & Moser (1987), such coherent structures have been studied extensively in both experiments and numerical simulations (Robinson 1991; Adrian 2007).

It is widely accepted that, at low Reynolds number, wall turbulence is dominated by the streaks and quasi-streamwise vortices characteristic of the near-wall cycle, which have streamwise length and spanwise spacing of approximately 10^3 and 10^2 wall units, respectively. The generation of these near-wall coherent structures is approximately periodic, as explained in the cyclic models proposed by Hamilton, Kim & Waleffe (1995), Waleffe (1997) and Schoppa & Hussain (2002). Kawahara & Kida (2001) have also visualized this periodic process in a low Reynolds number turbulent Couette flow.

Recent efforts show that, as Reynolds number increases, larger coherent structures emerge in the logarithmic and outer regions of the flow (e.g. the so called very-large-scale and large-scale motions) and become increasingly important from an energetic and dynamic point of view (see e.g. Hutchins & Marusic 2007*a*; Monty *et al.* 2009; Marusic, Mathis & Hutchins 2010; Smits, McKeon & Marusic 2011). For instance, Hutchins & Marusic (2007*b*) show that the peak magnitude of the streamwise turbulence intensity increases with the Reynolds number due to the influence of the very-large-scale motions (VLSMs). Further, the VLSMs also appear to modulate the amplitude of the near-wall cycle (Marusic *et al.* 2010). As such, flow control at higher Reynolds number must consider the effect of these larger-scale coherent structures as well. For more information regarding the scaling and structure of VLSMs, readers are referred to Smits *et al.* (2011).

Over the past two decades, it has become increasingly clear that linear processes play an important role in dictating the dynamics of these coherent structures, and hence, in determining the efficacy of any control technique. Kim & Lim (2000) studied the role of linear and nonlinear processes in a turbulent channel flow by carrying out numerical experiments that eliminated either the linear or nonlinear coupling term. These experiments demonstrated that the near-wall turbulence decays without the presence of the linear coupling term (which enhances non-normality of the linearized Navier–Stokes system). At the same time, the near-wall streamwise vortices could not be reproduced with the proper length scales without the nonlinear convective terms. Thus, the formation of the near-wall structures requires the nonlinear term, but the maintenance of these structures relies on linear interactions. Based on these insights, Lim & Kim (2004) conducted a singular value decomposition (SVD) analysis of the linearized Navier–Stokes system, modified to account for opposition control (Choi *et al.* 1994), and obtained results similar to those found in DNS or large eddy simulation (LES). These results, among others, imply that analyses based on the linearized Navier–Stokes equation give useful insights, even if they cannot entirely reproduce the coherent structures found in turbulent flows.

Despite this limitation, such linearized analyses offer significant advantages over DNS in the preliminary design and development of control methods as

well as understanding the underlying mechanisms due to their low computational expense. This is especially true at higher Reynolds numbers, for which DNS can be prohibitively expensive.

1.3. *Resolvent analysis and the objective of the present study*

The resolvent formulation proposed recently by McKeon & Sharma (2010) is conceptually similar to the SVD analysis of Lim & Kim (2004). However, it has some important differences in that the linearized system is continuously forced by the nonlinear term, and that it enables an evaluation of control in wavenumber–frequency space (i.e. spatio-temporal modes) at low computational cost. More specifically, the resolvent analysis treats the Fourier transformed Navier–Stokes equations as a forcing–response system: the nonlinear convective terms are considered as the forcing (input) to the system and the turbulent velocity is the response (output). The turbulent velocity and pressure fields are expressed as a linear superposition of propagating Fourier modes, identified via a gain-based decomposition (i.e. SVD) of the forcing–response transfer function: the resolvent operator. This decomposition enables targeted analyses of the effects of control on spatio-temporal modes resembling important coherent structures, such as the near-wall (NW) re-generation cycle and VLSMs. Details of the resolvent analysis are provided in § 2.1 below.

Previous studies have demonstrated that the resolvent formulation captures many of the key statistical and structural features of wall turbulence (see e.g. McKeon, Jacobi & Sharma 2013; Moarref *et al.* 2013; Sharma & McKeon 2013). In addition, the resolvent formulation is also emerging as a powerful tool for the analysis of specific control techniques for skin friction reduction. For example, Luhar, Sharma & McKeon (2014) investigated the effect of opposition control in turbulent pipe flow, while Luhar, Sharma & McKeon (2015) and Luhar, Sharma & McKeon (2016) studied the effect of compliant surfaces in turbulent channel flow. These studies demonstrated that the resolvent analysis is able to reproduce trends observed in DNS and LES with minimal computation (although there are quantitative differences).

The present work is an extension of the study carried out by Luhar *et al.* (2014): we investigate the effect of suboptimal control on coherent structures. The remainder of this paper is organized as follows. Outlines of the resolvent analysis and the suboptimal control theory proposed by Lee *et al.* (1998) are presented in § 2. The effect of suboptimal control on modes resembling the NW cycle and VLSMs is considered in § 3. Further discussion is presented in § 4. In particular, we compare the present results with those obtained in previous DNS. We also compare and contrast the effects of suboptimal control and opposition control within the resolvent framework. Finally, conclusions are drawn in § 5.

2. Approach

2.1. *Resolvent analysis*

In this section, we briefly review the resolvent formulation proposed by McKeon & Sharma (2010) and the procedure used by Luhar *et al.* (2015). The problem under consideration is a fully developed incompressible turbulent channel flow governed by the continuity equation and Navier–Stokes equation, i.e.

$$\boldsymbol{\nabla}\cdot\boldsymbol{u}=0, \tag{2.1}$$

$$\frac{\partial \boldsymbol{u}}{\partial t}=-\boldsymbol{\nabla}p-\boldsymbol{u}\cdot\boldsymbol{\nabla}\boldsymbol{u}+\frac{1}{Re_\tau}\nabla^2\boldsymbol{u}, \tag{2.2}$$

where $\boldsymbol{u} = [u\ v\ w]^{\mathrm{T}}$ represents the velocity with u, v and w being the streamwise (x), wall-normal (y) and spanwise (z) components, p is the pressure, t is the time and $Re_\tau = u_\tau^\sharp h^\sharp/\nu^\sharp$ is the friction Reynolds number, Here, the quantities are made dimensionless using the channel half-width $h^\sharp$ and the friction velocity $u_\tau^\sharp$. Note that, a superscript $\sharp$ represents dimensional variables and a superscript $+$ is used to denote normalization with respect to $u_\tau^\sharp$ and the kinematic viscosity $\nu^\sharp$.

For a fully developed turbulent channel flow, the velocity and pressure fields can be expressed as a superposition of Fourier modes with streamwise wavenumber k_x, spanwise wavenumber k_z and temporal frequency ω:

$$\begin{bmatrix}\boldsymbol{u}(x,y,z,t)\\ p(x,y,z,t)\end{bmatrix} = \int\int\int_{-\infty}^{\infty}\begin{bmatrix}\boldsymbol{u}_{\boldsymbol{k}}(y)\\ p_{\boldsymbol{k}}(y)\end{bmatrix} \mathrm{e}^{\mathrm{i}(k_x x + k_z z - \omega t)}\,\mathrm{d}k_x\,\mathrm{d}k_z\,\mathrm{d}\omega, \tag{2.3}$$

where $\mathrm{i} = (-1)^{1/2}$ and $[\boldsymbol{u}_{\boldsymbol{k}} p_{\boldsymbol{k}}]^{\mathrm{T}} = [u_{\boldsymbol{k}} v_{\boldsymbol{k}} w_{\boldsymbol{k}} p_{\boldsymbol{k}}]^{\mathrm{T}}$ are Fourier coefficients for the velocity and pressure fields, which vary in the non-homogeneous y direction. Each wavenumber–frequency combination $\boldsymbol{k} = (k_x, k_z, \omega)$ (or wavenumber–propagating speed combination $\boldsymbol{k} = (k_x, k_z, c)$) indicates a flow structure with streamwise wavelength $\lambda_x = 2\pi/k_x$ and spanwise wavelength $\lambda_z = 2\pi/k_z$ propagating downstream at speed $c = \omega/k_x$.

Based on this Fourier transformation, at each $\boldsymbol{k}$, we can express the Navier–Stokes equations for turbulent channel flow as

$$\boldsymbol{\nabla}_{\boldsymbol{k}} \cdot \boldsymbol{u}_{\boldsymbol{k}} = 0, \tag{2.4}$$

$$(-\mathrm{i}\omega + \mathrm{i}k_x U)\boldsymbol{u}_{\boldsymbol{k}} + (\partial U/\partial y)v_{\boldsymbol{k}}\boldsymbol{e}_{\boldsymbol{x}} + \boldsymbol{\nabla} p_{\boldsymbol{k}} - Re_\tau^{-1}\nabla_{\boldsymbol{k}}^2 \boldsymbol{u}_{\boldsymbol{k}} = \boldsymbol{f}_{\boldsymbol{k}}. \tag{2.5}$$

Here, $\boldsymbol{\nabla}_{\boldsymbol{k}} = [\mathrm{i}k_x\ \partial/\partial y\ \mathrm{i}k_z]^{\mathrm{T}}$ and $\nabla_{\boldsymbol{k}}^{\mathrm{T}}$ represent the gradient and divergence operators, and $\boldsymbol{f}_{\boldsymbol{k}} = (-u\cdot\boldsymbol{\nabla}u)_{\boldsymbol{k}}$ represents the Fourier transformed nonlinear term. $U(y)$ represents the mean velocity profile.

These equations can be rearranged into the following forcing–response (or input–output) relationship:

$$\begin{bmatrix}\boldsymbol{u}_{\boldsymbol{k}}\\ p_{\boldsymbol{k}}\end{bmatrix} = \left(-\mathrm{i}\omega\begin{bmatrix}\boldsymbol{I} & \\ & 0\end{bmatrix} - \begin{bmatrix}\boldsymbol{L}_{\boldsymbol{k}} & -\boldsymbol{\nabla}_{\boldsymbol{k}}\\ \nabla_{\boldsymbol{k}}^{\mathrm{T}} & 0\end{bmatrix}\right)^{-1}\begin{bmatrix}\boldsymbol{I}\\ 0\end{bmatrix}\boldsymbol{f}_{\boldsymbol{k}} \tag{2.6}$$

$$= \underbrace{\boldsymbol{H}_{\boldsymbol{k}}}_{\textit{resolvent operator}}\ \boldsymbol{f}_{\boldsymbol{k}}, \tag{2.7}$$

where

$$\boldsymbol{L}_{\boldsymbol{k}} = \begin{bmatrix}-\mathrm{i}k_x U + Re_\tau^{-1}\nabla_{\boldsymbol{k}}^2 & -(\partial U/\partial y) & 0\\ 0 & -\mathrm{i}k_x U + Re_\tau^{-1}\nabla_{\boldsymbol{k}}^2 & 0\\ 0 & 0 & -\mathrm{i}k_x U + Re_\tau^{-1}\nabla_{\boldsymbol{k}}^2\end{bmatrix}, \tag{2.8}$$

$$\nabla_{\boldsymbol{k}}^2 = -k_x^2 - (\partial^2/\partial y^2) - k_z^2. \tag{2.9}$$

Here, the nonlinear term $\boldsymbol{f}_{\boldsymbol{k}}$ is identified as a forcing term to the linear Navier–Stokes system and the resolvent operator $\boldsymbol{H}_{\boldsymbol{k}}$, which depends on the linear operator $\boldsymbol{L}_{\boldsymbol{k}}$, translates this forcing into a velocity and pressure response: $[\boldsymbol{u}_{\boldsymbol{k}}\ p_{\boldsymbol{k}}]^{\mathrm{T}}$.

A singular value decomposition (SVD) of the resolvent operator $\boldsymbol{H}_{\boldsymbol{k}}$ identifies an ordered set of orthonormal forcing and response modes for each wavenumber–speed combination $\boldsymbol{k}$ under an L^2 energy norm:

$$\boldsymbol{H}_{\boldsymbol{k}} = \sum_m \boldsymbol{u}_{\boldsymbol{k},m}\sigma_{\boldsymbol{k},m}\boldsymbol{f}_{\boldsymbol{k},m}{}^{*}. \tag{2.10}$$

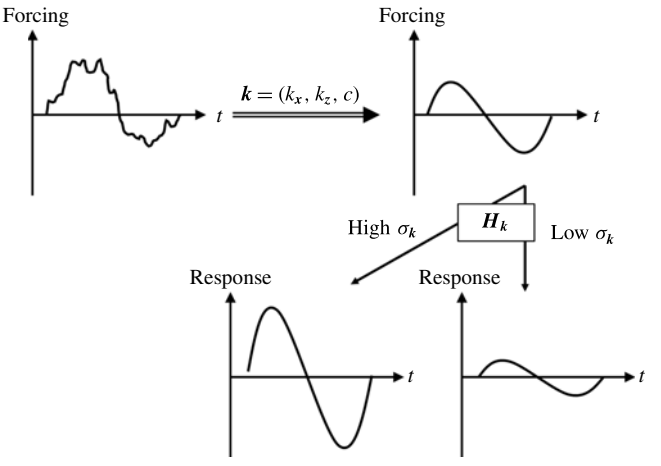

FIGURE 1. A conceptual illustration of the resolvent analysis.

where

$$\sigma_{\boldsymbol{k},1} \gg \sigma_{\boldsymbol{k},2} > \cdots > \sigma_{\boldsymbol{k},m} > \cdots > 0, \tag{2.11}$$

$$\int_{-1}^{1} \boldsymbol{f}^{*}_{\boldsymbol{k},l} \boldsymbol{f}_{\boldsymbol{k},m} \,\mathrm{d}y = \delta_{lm}, \tag{2.12}$$

$$\int_{-1}^{1} \boldsymbol{u}^{*}_{\boldsymbol{k},l} \boldsymbol{u}_{\boldsymbol{k},m} \,\mathrm{d}y = \delta_{lm}. \tag{2.13}$$

Here, δ denotes the Kronecker delta and a superscript of $*$ denotes the complex conjugate.

From (2.10)–(2.13), it is evident that the mth forcing mode yields the mth velocity–pressure response mode, amplified by the singular value $\sigma_{k,m}$, as conceptually illustrated in figure 1. For instance, forcing $\boldsymbol{f}_{\boldsymbol{k},1}$ leads to a response $\sigma_{\boldsymbol{k},1}[\boldsymbol{u}_{\boldsymbol{k},1}\ p_{\boldsymbol{k},1}]^{\mathrm{T}}$. It is worth noting that for $\boldsymbol{k}$ combinations relevant to real flows the resolvent operator is often low rank: the first singular value tends to be much larger than the rest (2.11). In other words, the first singular mode (rank-1 mode) is expected to dominate the turbulent flow field. Indeed, previous studies (McKeon & Sharma 2010; McKeon *et al.* 2013; Moarref *et al.* 2013) have shown that models based on this rank-1 approximation yield predictions for turbulent statistics and coherent structure consistent with observations. Following these findings, Luhar *et al.* (2014) and Luhar *et al.* (2015) consider only these rank-1 modes to analyse the effect of control on wall turbulence. Similarly, we only consider rank-1 modes and singular values at each $\boldsymbol{k}$ in the remainder of this manuscript: $[\boldsymbol{u}_{\boldsymbol{k}}\ p_{\boldsymbol{k}}]^{\mathrm{T}} = [\boldsymbol{u}_{\boldsymbol{k},1}\ p_{\boldsymbol{k},1}]^{\mathrm{T}}$ and $\sigma_{\boldsymbol{k}} = \sigma_{\boldsymbol{k},1}$.

Note that the resolvent analysis procedure presented in (2.6)–(2.13) does not consider just the linearized Navier–Stokes equations. The analysis assumes that the nonlinearity supports the base flow (i.e. the mean velocity profile in the resolvent operator) via the mean Reynolds stress, and forces the fluctuating velocity and pressure responses via the time-varying Reynolds stresses. Consistent with the findings of Kim & Lim (2000), this means that a complete quantitative description of the turbulent velocity and pressure fields requires knowledge of the nonlinear interaction between modes. However, even without this information, the resolvent framework permits analysis of control techniques on a mode-by-mode basis, in a forcing-normalized sense. This is discussed in greater detail in § 2.3.

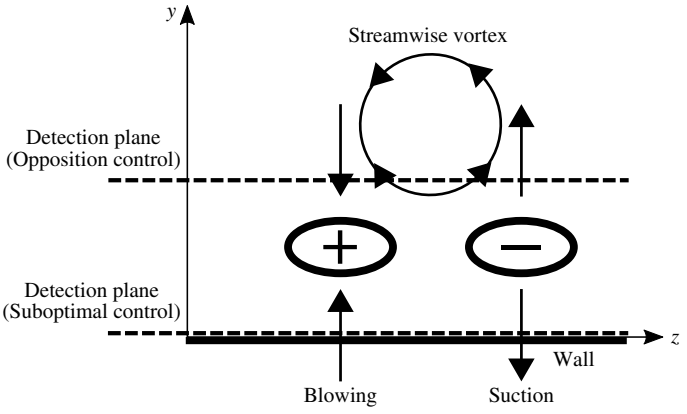

FIGURE 2. Schematic of the suboptimal control method.

2.2. *Suboptimal control laws*

As shown in figure 2, the opposition control technique proposed by Choi *et al.* (1994) generates blowing and suction at the wall to oppose the wall-normal velocity measured at a 'virtual detection plane' located above wall in order suppress the quasi-streamwise vortices associated with the NW cycle. At low Reynolds numbers, this yields more than 20 % drag reduction in DNS.

Recognizing that the requirement of sensor information away from the wall may be impractical, Lee *et al.* (1998) sought to develop control laws similar to opposition control that only required sensor information at the wall, i.e. the shear stress or pressure. These control laws were determined by analytical solutions that minimized physically intuitive cost functions for discretized versions of the governing equations. Based on observations that opposition control led to an enhancement of the fluctuating spanwise shear stress at the wall, the following cost function was used for the case where $(\partial w/\partial y)_w$ was used as the sensed quantity,

$$J_{SP}(\phi) = \frac{\ell}{2A\Delta t}\int_S\int_t^{t+\Delta t}\phi^2\,\mathrm{d}t\,\mathrm{d}S - \frac{1}{2A\Delta t}\int_S\int_t^{t+\Delta t}\underbrace{\left(\frac{\partial w}{\partial y}\right)_w^2}_{\textit{spanwise wall-shear}}\mathrm{d}t\,\mathrm{d}S. \tag{2.14}$$

Here, ϕ represents the wall-normal velocity at the wall used as the control input, A is the area of wall, Δt is the short time span for optimization and ℓ is the relative cost of the actuation. The derived control law was expressed in the Fourier domain as

$$\phi_{\boldsymbol{k}} = \alpha\frac{\mathrm{i}k_z}{K}\left(\frac{\partial w_{\boldsymbol{k}}}{\partial y}\right)_w, \tag{2.15}$$

where $K = (k_x^2 + k_z^2)^{1/2}$ and α is a coefficient determining the blowing and suction magnitude. Lee *et al.* (1998) carried out DNS of channel flow at $Re_\tau = 110$, and obtained 22 % drag reduction using this control law. For the case where the streamwise wall shear $(\partial u/\partial y)_w$ was used as the control input, the control law, derived using the same procedure as (2.15), was expressed as

$$\phi_{\boldsymbol{k}} = -\alpha\frac{\mathrm{i}k_x}{K}\left(\frac{\partial u_{\boldsymbol{k}}}{\partial y}\right)_w. \tag{2.16}$$

However, the friction drag was reported to increase with this control law. Note that, for both cases, the magnitude of the blowing and suction (α) was tuned to ensure that the root-mean-square value (r.m.s.) of ϕ matched the r.m.s. of the wall-normal velocity at $y^+ \approx 10$.

In this paper, we assess the suboptimal control laws shown in (2.15) and (2.16), which are hereafter denoted as Case SP and Case ST, respectively. The effect of suboptimal control is included in the resolvent operator $\boldsymbol{H_k}$ as a boundary condition for the upper ($y=+1$) and lower ($y=-1$) walls. The no-slip condition is employed for the uncontrolled case. The complete boundary conditions for the suboptimal control laws at a wavenumber–speed combination $\boldsymbol{k}$ are expressed as follows:

$$\text{[Case SP]}: \quad (u_{\boldsymbol{k}})_w = (w_{\boldsymbol{k}})_w = 0, \quad (v_{\boldsymbol{k}})_w = \phi_{\boldsymbol{k}} = \alpha \frac{\mathrm{i}k_z}{K} \left(\frac{\partial w_{\boldsymbol{k}}}{\partial y} \right)_w, \tag{2.17a,b}$$

$$\text{[Case ST]}: \quad (u_{\boldsymbol{k}})_w = (w_{\boldsymbol{k}})_w = 0, \quad (v_{\boldsymbol{k}})_w = \phi_{\boldsymbol{k}} = -\alpha \frac{\mathrm{i}k_x}{K} \left(\frac{\partial u_{\boldsymbol{k}}}{\partial y} \right)_w. \tag{2.18a,b}$$

Finally, it is worth mentioning that the blowing and suction magnitude α is essentially a length scale (i.e. $\alpha^+ = \alpha Re_\tau$).

2.3. *Resolvent-based assessment of suboptimal control*

As mentioned in §§ 2.1 and 2.2, we follow the procedure used by Luhar *et al.* (2015) to assess how suboptimal control affects resolvent modes that serve as models for the dynamically important coherent structures. In the framework of resolvent mode analysis, there are two primary measures to assess the effectiveness of control. The first measure is the forcing–response gain, i.e. the singular value $\sigma_{\boldsymbol{k}}$, itself. If the singular value in the controlled case decreases relative to that in the no-control case, the mode is suppressed by the control; if it increases, the mode is amplified. The second measure is the Reynolds shear stress contribution (Luhar *et al.* 2015):

$$R_{\boldsymbol{k}} = \int_{-1}^{1} \sigma_{\boldsymbol{k}}^2 \ \mathrm{Re}(u_{\boldsymbol{k}}{}^* v_{\boldsymbol{k}})(+y)\, \mathrm{d}y, \tag{2.19}$$

(where Re(··) denotes the real component), which is based on the Fukagata–Iwamoto–Kasagi (FIK) identity (Fukagata *et al.* 2002). Note that (2.19) represents a forcing-normalized quantity; it assumes that the velocity response at a wavenumber–propagating speed contribution $\boldsymbol{k}$ is given by $\sigma_{\boldsymbol{k}} \boldsymbol{u}_{\boldsymbol{k}}$.

Of course, both these measures neglect the effect of control on the nonlinear forcing term, which arises from mode–mode interactions. As noted in § 1.2, while linear mechanisms are essential for maintaining near-wall turbulence, the nonlinear term plays an important role in the formation of the near-wall cycle (e.g. Kim & Lim 2000). However, due to its conservative nature, the nonlinear term does not dissipate or generate turbulent kinetic energy, but merely serves to transfer energy across spectral space. Turbulent kinetic energy is generated via the action of the vertical fluctuating velocity on the mean shear $v_k(\mathrm{d}U/\mathrm{d}y)$ (e.g. Chernyshenko & Baig 2005); this is a linear mechanism that is captured by the resolvent operator as shown in (2.6)–(2.9). In other words, energy transfer from the mean flow to the turbulence is reflected in the forcing–response gain singular value $\sigma_{\boldsymbol{k}}$. Therefore, the conservative nature of the nonlinearity suggests that if a control technique suppresses singular values and Reynolds stress contributions across spectral space, then it is likely to be effective in suppressing turbulence regardless of nonlinear effects.

2.4. *Numerical details*

The Chebyshev collocation method (Weideman & Reddy 2000) is used for discretization in the wall-normal direction. The mean velocity profile $U(y)$ in the linear operator $\boldsymbol{L_k}$ (in the resolvent operator $\boldsymbol{H_k}$) is obtained by using the turbulent viscosity model proposed by Reynolds & Tiederman (1967). To test whether the exact form of the mean profile led to a substantial difference in results, we also repeated the analysis for a limited subset of modes with uncontrolled and controlled (for Case SP) mean profiles obtained in DNS. The results obtained using the mean profiles from DNS were in good agreement with the results obtained using the mean profile computed using the eddy viscosity model. For example, singular values with and without control changed by less than 6 % for modes resembling the near-wall cycle. These results suggest that the model predictions reported below are not very sensitive to the exact form of the mean velocity profile.

Luhar *et al.* (2015) conducted the resolvent mode analysis in the lower half-channel only to avoid the so-called pairing (Moarref *et al.* 2013) and to make the computation more efficient. In turn, one must carefully specify the symmetry of each mode. In the present study, in contrast, we compute the whole channel to avoid this complexity. We have confirmed excellent agreement for rank-1 modes (which are of interest in the present work) in the uncontrolled case between the results computed in the whole channel and the half-channel using the user-specified symmetry.

Investigation on the grid number (N) dependency in the uncontrolled case showed that the relative error of the Reynolds shear stress contribution $R_{\boldsymbol{k}}$ between the cases with $N = 240$ $(= 2 \times 120)$ and $N = 1000$ (2×500) was of the order of 10^{-4} per cent. Further, for the controlled case, the relative difference of $R_{\boldsymbol{k}c}/R_{\boldsymbol{k}0}$ between $N = 240$ and $N = 1000$ depends on the blowing and suction magnitude α^+: the difference is of the order of 0.1 %, approximately 1 % and 2 % for $\alpha^+ = 1$, 10 and 100, respectively. Therefore, we use $N = 240$ and $N = 400$ in the rest of the paper. We use $N = 400$ only when we plot the wall-normal profiles (e.g. figure 4). Note that this is comparable to typical DNS resolutions for $Re_\tau < O(1000)$.

3. Results

In the present study, we focus on how control affects resolvent modes resembling the near-wall coherent structure (NW cycle) and VLSMs. As mentioned in § 1.2, the dynamic importance of these structures has been highlighted in many previous studies, which suggests that targeting such modes is central to the development of effective control.

Following prior resolvent-based analyses (McKeon & Sharma 2010; McKeon *et al.* 2013; Sharma & McKeon 2013; Luhar *et al.* 2015), we consider the wavenumber–propagating speed combination $\boldsymbol{k} = (k_x, k_z, c^+) \approx (12, 120, 10)$ at $Re_\tau = 2000$ or $\boldsymbol{k} = (k_x, k_z, c^+) \approx (0.66, 6.6, 10)$ at $Re_\tau = 110$, corresponding to wavelengths $\lambda_x^+ = 2\pi Re_\tau/k_x \approx 10^3$ and $\lambda_z^+ = 2\pi Re_\tau/k_z \approx 10^2$, as the modes that represent the near-wall cycle (NW modes). Note that $k_z^+ > 0$ represents oblique waves that propagate in the positive z direction, while $k_z^+ < 0$ represents oblique waves that propagative in the negative z direction. Apart from this directionality, both modes are structurally similar due to the spanwise homogeneity of the flow.

To capture the dynamics of VLSMs, we consider the wavenumber–propagating speed combination $\boldsymbol{k} = (k_x, k_z, c^+) \approx (1, 10, 16)$ at $Re_\tau = 2000$. This mode represents flow structures with $\lambda_x^+ \approx 6h^+$, $\lambda_z^+ \approx 0.6h^+$, and a propagation speed approximately two thirds of the centreline velocity. These length and velocity scales were chosen

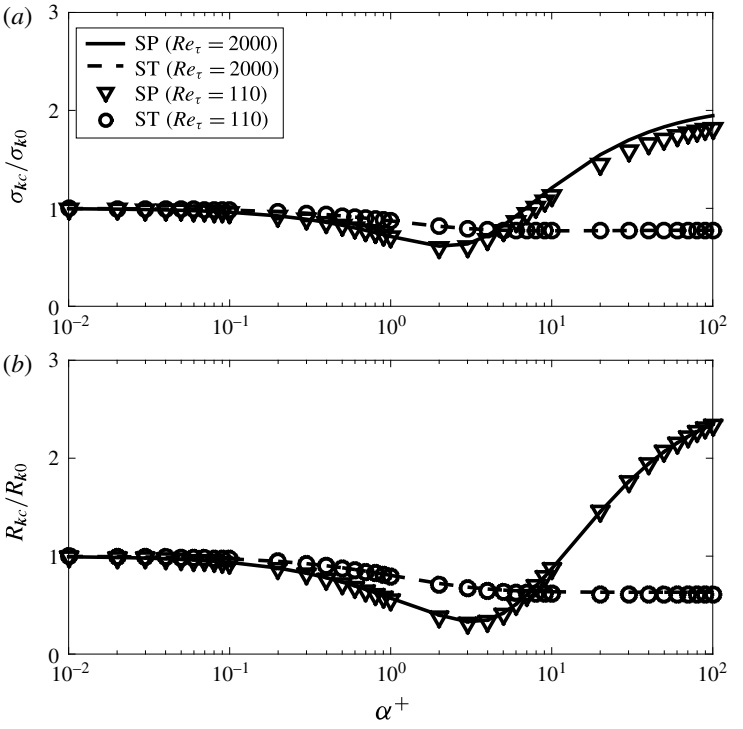

FIGURE 3. Relationship between the blowing and suction magnitude α^+ and the ratio of controlled to uncontrolled cases for NW modes: (*a*) singular value σ_{kc}/σ_{k0}; (*b*) Reynolds shear stress contribution R_{kc}/R_{k0}. Solid lines, Case SP ($Re_\tau = 2000$); dashed lines, Case ST ($Re_\tau = 2000$). Triangle, Case SP ($Re_\tau = 110$); circle, Case ST ($Re_\tau = 110$).

based on previous experimental measurements and modelling results. For example, the boundary layer measurements made by Hutchins & Marusic (2007*a*) showed the presence of a local peak in the streamwise velocity spectrum for structures of length $\lambda_x \approx 6h$ near wall-normal location $y \approx 0.06h$ at $Re_\tau = 1910$. Resolvent modes tend to localize near their critical layer, which is defined as the location where the mode speed matches the local mean velocity (McKeon & Sharma 2010). For propagation speed $c^+ = 16$, this corresponds to $y_c^+ \approx 105$, or $y_c/h \approx 0.05$ at $Re_\tau = 2000$.

3.1. *Effect of control on the near-wall modes*

First, we focus on the NW modes. Figure 3 shows the relationship between the blowing and suction magnitude α^+ and ratio of controlled to uncontrolled singular values (figure 3*a*) and Reynolds shear stress contributions (figure 3*b*). Consistent with previous studies (Luhar *et al.* 2014, 2015), there is close correspondence between the singular value and the Reynolds shear stress contribution. Solid lines in figure 3, which represent Case SP (i.e. control based on spanwise shear) at $Re_\tau = 2000$, show that the maximum reduction of σ_k is achieved at $\alpha^+ \approx 2$ ($\sigma_{kc}/\sigma_{k0} \approx 0.61$, $R_{kc}/R_{k0} \approx 0.40$), maximum reduction of R_k is achieved at $\alpha^+ \approx 4$ ($\sigma_{kc}/\sigma_{k0} \approx 0.72$, $R_{kc}/R_{k0} \approx 0.35$) and drag increases for $\alpha^+ > 10^1$. Case ST (control based on streamwise shear; dashed lines) shows drag reduction too, but there is little dependency on blowing and suction magnitude α^+ once the effects of control become significant

($\alpha^+ \geqslant 10^1$). Surprisingly, Case ST was reported to increase the drag in DNS at $Re_\tau = 110$ by Lee *et al.* (1998). We will discuss this discrepancy in detail in § 4.1.2.

Note that there is close correspondence between the lines and the markers (triangle or circle) in figure 3, which suggests that the predictions are not very sensitive to Reynolds numbers, at least within the range tested ($Re_\tau = 110$–2000). In other words, the effect of control on the NW coherent structures does not change with increasing Re_τ. At first glance, this appears to contradict many previous studies which show that control performance deteriorates with Reynolds number. However, as discussed in later sections (see §§ 4.1.3 and 3.4), the deterioration in performance may be attributed to the fact that as Reynolds number increases, additional regions of spectral space become energetic, where control can have a harmful influence.

For both cases, the ratios σ_{kc}/σ_{k0} and R_{kc}/R_{k0} approach a constant value as α^+ increases in the figure 3. This is simply because the dynamics associated with the (large) feedback component dominates over the dynamics emerging from the original (uncontrolled) resolvent operator as α^+ increases. In other words, for low α^+, the blowing and suction interacts with and modifies the natural dynamics of the flow. However, for high α^+, blowing and suction overwhelms the natural dynamics. The magnitude of α^+ that effectively suppresses NW coherent structures is discussed further in § 4.1.1.

Based on the trends observed in figure 3, we focus on values of α^+ for Case SP at $Re_\tau = 2000$ that show salient behaviour (i.e. maximum drag reduction/increment) and consider the effect of control on mode structure. Figure 4 shows the profile of velocity amplitudes and Reynolds shear stress. The effects of control start to appear at $\alpha^+ = 0.44$. For this case, the peak of controlled wall-normal velocity ($|v_{kc}|$) is a little larger than that for the uncontrolled case (see figure 4*a*,*b*). At the same time, the well-known 'virtual wall' starts to form, which mitigates vertical momentum transport and reduces the effect of linear coupling (Kim & Lim 2000). Here, the presence of virtual wall is indicated by the sudden fall of the magnitude of wall-normal velocity. Maximum suppression of singular value is attained at $\alpha^+ = 2.0$, at which point, we can clearly observe the establishment of a virtual wall. The peak location of streamwise velocity is shifted above the critical layer y_c^+, where the mode speed matches the local mean velocity $U^+(y_c^+) = c^+$ (figure 4*c*). Despite the strong suppression of singular value, the normalized Reynolds shear stress increases relative to the uncontrolled case (figure 4*d*). However, the Reynolds shear stress contribution, as defined in (2.19), is suppressed because it is proportional to σ_k^2. The Reynolds shear stress contribution is suppressed most at $\alpha^+ = 4.0$. For this case, we can observe a virtual wall-like velocity drop at $y^+ \approx 10$ (figure 4*e*, *f*) and the wall-normal velocity at the wall (i.e. control input) is as high as the peak value. The peak normalized Reynolds shear stress is also substantially lower. Based on these observations, we suggest that the effect of Case SP is essentially similar to that of opposition control. Note that the controlled streamwise velocity is shifted further toward the wall as the actuation amplitude increases from $\alpha^+ = 2.0$ to $\alpha^+ = 4.0$: we discuss this point further in § 4.2. Figure 4(*g*,*h*) shows velocity and Reynolds stress profile for the case of drag increment at $\alpha^+ = 10^2$; the peak locations of controlled streamwise velocity and Reynolds shear stress are shifted toward the wall, from which we can assume more shear stress is generated at the wall when the control is applied. This is also consistent with our earlier observation that, for large blowing and suction, the natural dynamics of the mode is overwhelmed by the actuation.

Figure 5 shows predicted velocity fields in the spanwise wall-normal plane. Here, the velocity structure includes contributions from both oblique modes ($k_z > 0$ and

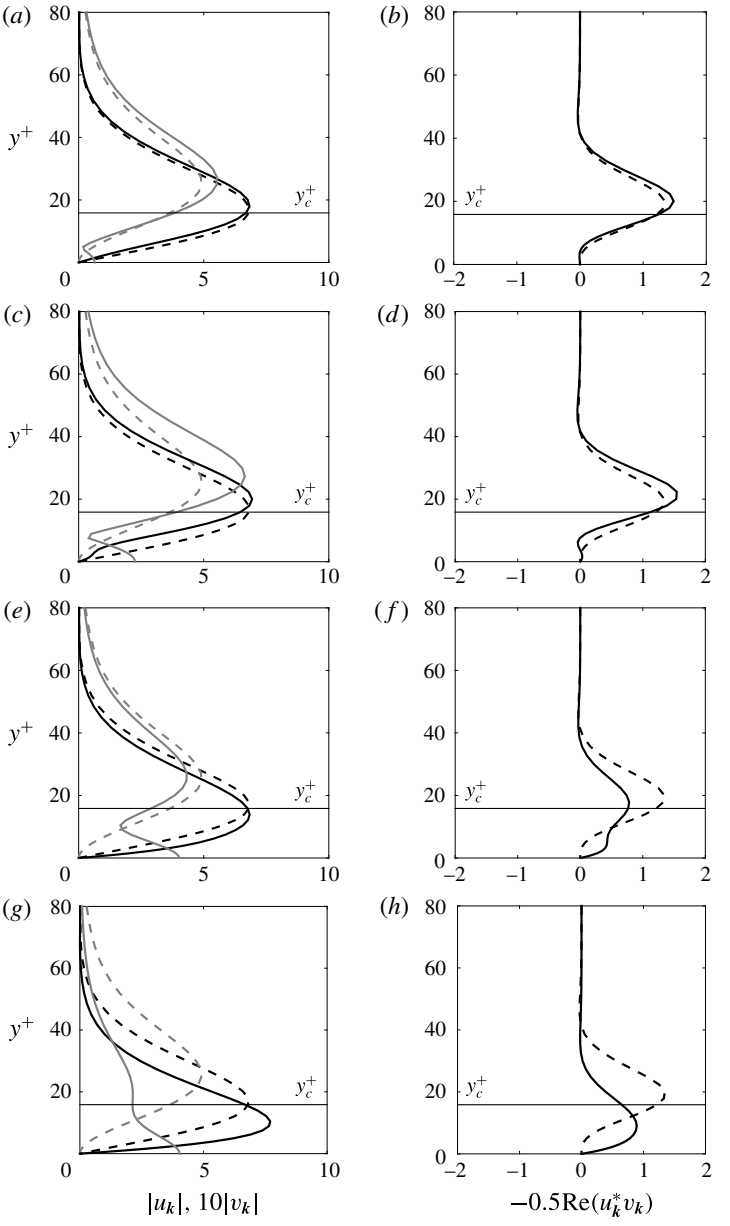

FIGURE 4. Profiles showing wall-normal variations in structure for resolvent modes resembling the NW cycle at $Re_\tau = 2000$: (*a*,*c*,*e*,*g*) amplitude of streamwise velocity (black lines) and wall-normal velocity (grey lines); (*b*,*d*,*f*,*h*) Reynolds shear stress. Dashed lines, uncontrolled; solid lines, controlled (Case SP). (*a*,*b*) $\alpha^+ = 0.44$; (*c*,*d*) $\alpha^+ = 2.0$; (*e*,*f*) $\alpha^+ = 4.0$; (*g*,*h*) $\alpha^+ = 10^2$. Black horizontal line indicates the location of critical layer, $y_c^+ \approx 16$.

$k_z < 0$). Note that these figures show the cross-section where the magnitude of the streamwise velocity is maximum: since the resolvent formulation yields periodic flow structures, maxima and minima occur at intervals of $\lambda_x^+/2$ in the streamwise direction.

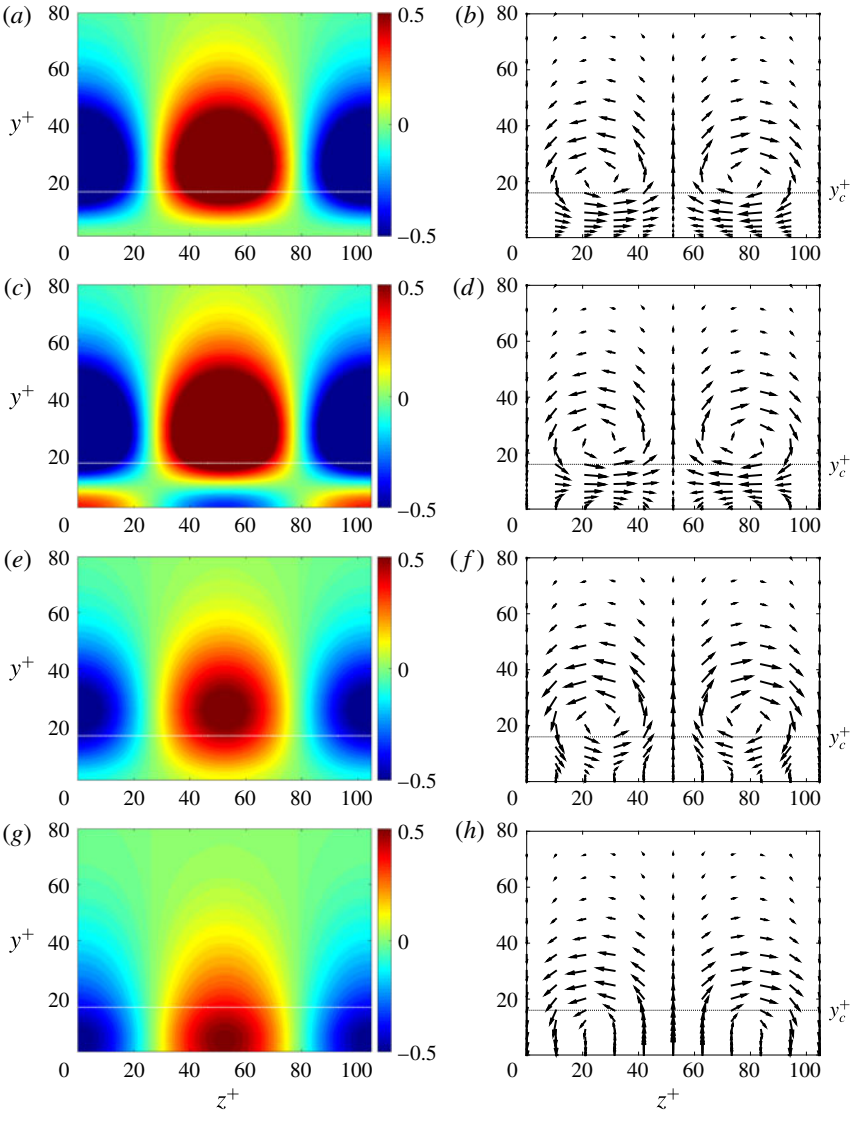

FIGURE 5. (Colour online) Velocity structure for NW modes in the spanwise wall-normal plane at $Re_\tau = 2000$: (*a*,*c*,*e*,*g*) wall-normal velocity amplitude; (*b*,*d*,*f*,*h*) wall-normal and spanwise velocity field. (*a*,*b*) no control; (*c*,*d*) $\alpha^+ = 2.0$; (*e*,*f*) $\alpha^+ = 4.0$; (*g*,*h*) $\alpha^+ = 10^2$. The horizontal dashed lines show the critical layer location, $y_c^+ \approx 16$.

Figure 5(*a*,*b*) shows the uncontrolled case. The presence of periodic sweeps and ejections and counter-rotating streamwise vortices is consistent with known features of the NW cycle, confirming that this resolvent mode serves as a useful model for these dynamically important coherent structures. For control with $\alpha^+ = 2.0$ (figure 5*c*,*d*), a virtual wall ($v \approx 0$) is clearly observed at $y^+ \approx 10$ in accordance with figure 4(*c*). On the other hand, figure 5(*e*,*f*) reveals that a virtual wall-like velocity drop observed in figure 4(*e*) was not a virtual wall, even though this case ($\alpha^+ = 4.0$) corresponds to the maximum reduction of Reynolds shear stress contribution: we discuss this

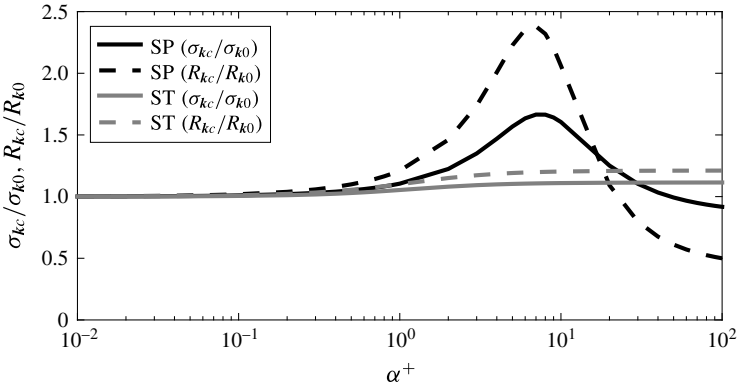

FIGURE 6. Relationship between the blowing and suction magnitude α^+ and drag contribution of the mode resembling VLSMs at $Re_\tau = 2000$. Black lines, Case SP; grey lines, Case ST. Solid lines, σ_{kc}/σ_{k0}; dashed lines, R_{kc}/R_{k0}.

point further in § 4.2. Figure 5(*g*,*h*) shows the case where performance deteriorates ($\alpha^+ = 10^2$). Due to the strong blowing and suction, the magnitude of the wall-normal velocity is highest at the wall and structure in the spanwise wall-normal plane suggests that the quasi-streamwise vortices are partially 'absorbed' into the wall.

3.2. *Effect of control on the very-large-scale motions*

Next, we investigate the effect of suboptimal control on resolvent modes resembling VLSMs. Figure 6 shows the relationship between the blowing and suction magnitude α^+ and the two ratios that quantify the effect of control, i.e. the singular value ratio σ_{kc}/σ_{k0} and the ratio of Reynolds shear stress contribution R_{kc}/R_{k0}. For Case SP (black line), R_{kc}/R_{k0} increases after the control effect appears at $\alpha^+ > 10^{-1}$ and reaches a maximum value at $\alpha^+ = 7.0$. As α^+ increases further, R_{kc}/R_{k0} begins to decrease. Large reduction of R_k ($\approx$50 %) is achieved for $\alpha^+ \approx 10^2$. These observations contrast sharply with the α^+ dependence observed for the NW modes. For similar values of α^+, suboptimal control seems to have the opposite effect on modes resembling the VLSMs compared to modes resembling the NW cycle. This is discussed in greater detail below. Note that Case ST (black line) leads to a monotonic increase in the Reynolds shear stress contribution, and there is little dependence on the magnitude of blowing and suction above $\alpha^+ \geqslant 10^1$.

Figure 7 shows wall-normal profiles of each velocity component for VLSM-type modes at $Re_\tau = 2000$ for (i) the uncontrolled case, (ii) Case SP with blowing and suction amplitude $\alpha^+ = 7$, which leads to an increase and drag, and (iii) Case SP with $\alpha^+ = 10^2$, which leads to a drag decrease. Figure 8 shows the velocity structure associated with this mode in the y–z plane (cf. figure 5 for the NW modes). As expected, the peak of the streamwise velocity is located slightly above the critical layer $y_c^+ \approx 105$ for this mode (uncontrolled case in the figure 7*a*,*c*). As shown in figure 8(*a*), the flow structure associated with this mode comprises velocity fields that are periodic over the prescribed length scales $\lambda_x^+ \approx 6h^+$ and $\lambda_z^+ \approx 0.6h^+$, and give rise to large streamwise roll cells. Although the wall-normal velocity associated with this mode is much smaller than the streamwise velocity, the motions are clearly active in the sense that they contribute Reynolds shear stress (uncontrolled case in figure 7*a*,*b*). All of these characteristics are consistent with previous studies (e.g. Hutchins &

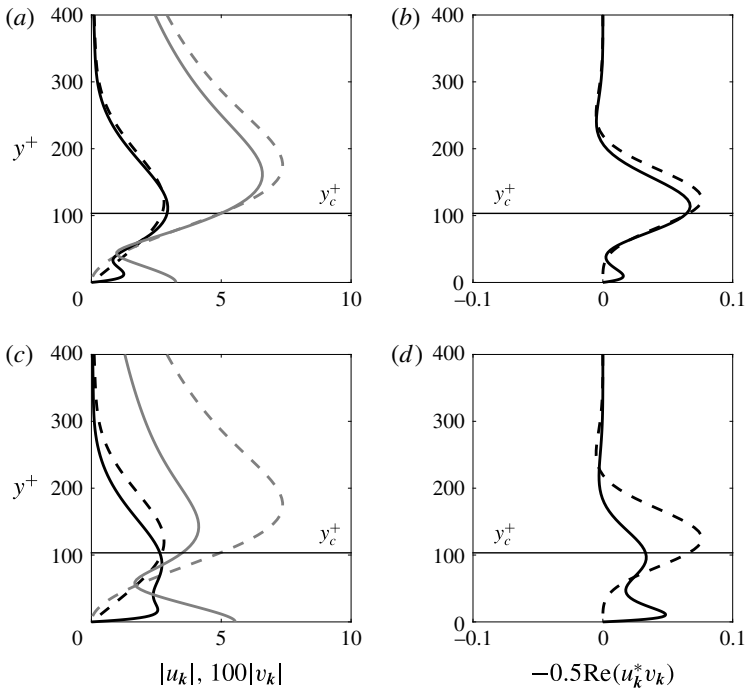

FIGURE 7. Wall-normal profiles for VLSM-type modes at $Re_\tau = 2000$: (*a*,*c*) amplitude of streamwise velocity (black lines) and wall-normal velocity (grey lines); (*b*,*d*) Reynolds shear stress. Dashed lines, no control; solid lines, controlled. (*a*,*b*) $\alpha^+ = 7.0$; (*c*,*d*) $\alpha^+ = 10^2$. Black horizontal line shows the location of critical layer, $y_c^+ \approx 105$.

Marusic 2007*a*; Smits *et al.* 2011), confirming that this large-scale resolvent mode can serve as a useful model in the evaluation of flow control for VLSMs.

In figure 7(*a*,*b*), for which the R_k increment is maximum (i.e. $\alpha^+ \approx 7$), the profiles of velocities amplitude and Reynolds shear stress remain nearly unchanged near and above the critical layer, although a virtual wall looks to be formed near the wall ($y^+ \approx 50$). This observation suggests that there is little control effect near and above the critical layer ($y_c^+ \approx 105$), which is the region considered important for drag reduction since localization around the critical layer leads to high singular values. Instead, blowing and suction simply generate additional turbulence near the wall. This is also evident in the predicted flow structure shown in figure 8(*b*). For the case where large R_k reduction is observed ($\alpha^+ = 10^2$), the peak magnitudes of the streamwise and wall-normal velocity are shifted towards the wall (figure 7*c*). Further, the normalized Reynolds shear stress is successfully suppressed near the critical layer, indicating a change in the phase relationship between the streamwise and wall-normal velocity components, but amplified close to the wall (figure 7*d*). From these observations, it can be postulated that effective control for VLSMs suppresses the Reynolds shear stress near, or above, the critical layer. Figure 8 shows that, for both $\alpha^+ = 7$ and $\alpha^+ = 10^2$, blowing and suction lead to the generation of a strong wall-normal velocity field that extends to $y^+ \leqslant 30$. For conditions in which drag is reduced (i.e. $\alpha^+ = 10^2$), the wall-normal velocity close to the critical layer is suppressed, and the streamwise roll cells are substantially weakened (figure 8*c*).

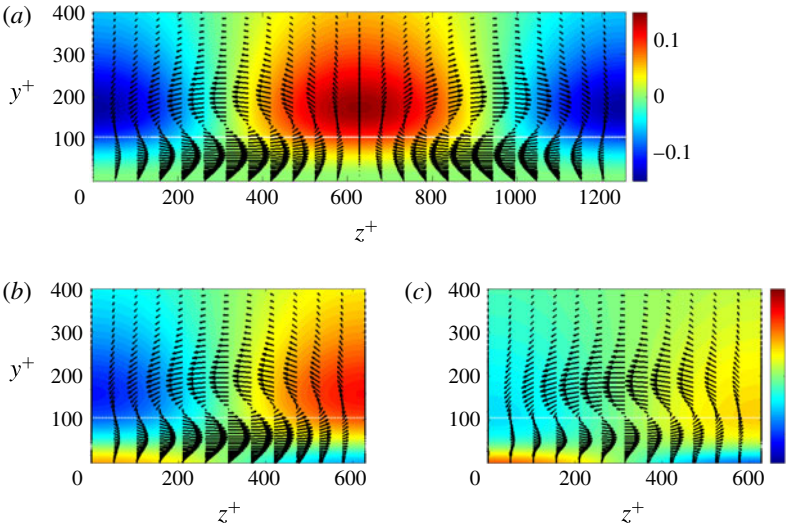

FIGURE 8. (Colour online) Velocity structure for VLSMs in the spanwise wall-normal plane at $Re_\tau = 2000$: contour, wall-normal velocity amplitude; arrows, wall-normal and spanwise velocity field. (*a*) no-control; (*b*) $\alpha^+ = 7$; (*c*) $\alpha^+ = 1 \times 10^2$. The horizontal dashed lines show the critical layer location, $y_c^+ \approx 105$.

As noted earlier, for a given value of α^+, suboptimal control has the opposite effect on NW modes and VLSMs. Together, the model predictions from §§ 3.1 and 3.2 suggest the following interpretation. For weak blowing and suction with $\alpha^+ < 1$, control effectively suppresses structures located very close to the wall (figure 4*a*) but has little effect on larger-scale structures resembling VLSMs present far from the wall. For moderate values of blowing and suction, $\alpha^+ \approx 1$–7, control suppresses the NW modes further but leads to harmful effects on larger-scale modes, i.e. the generation of additional turbulence near the wall. Finally, powerful blowing and suction (e.g. $\alpha^+ \approx 100$) successfully suppress modes resembling the VLSMs, but overwhelms structures close to the wall (see figures 5*h* and 7*d*).

Recall that the design parameter α^+ is essentially a length scale that translates the sensed wall shear stress into a blowing and suction velocity. As a result, it is not altogether surprising that large values of $\alpha^+ \geqslant O(10)$ are required to effectively interact with modes resembling VLSMs whose critical layer is located at $y_c^+ \approx 105$, while smaller values of $\alpha^+ = O(1)$ are sufficient for modes resembling the near-wall cycle with critical layer location $y_c^+ \approx 16$. Unfortunately, this also suggests that, for control to be effective across spectral space, a value of α^+ that varies with mode speed (or critical layer location) may be required. We consider such mode speed effects in the following section.

3.3. *Effect of propagation speed*

In this section, we investigate the effect of propagation speed c^+ to provide further insight into the effects of suboptimal control. Since high-gain resolvent modes tend to localize near the critical layer (McKeon & Sharma 2010), for modes with identical wavelengths, an increase in propagation speed also indicates an increase in the distance from the wall, where the sensing and actuation take place. Figure 9

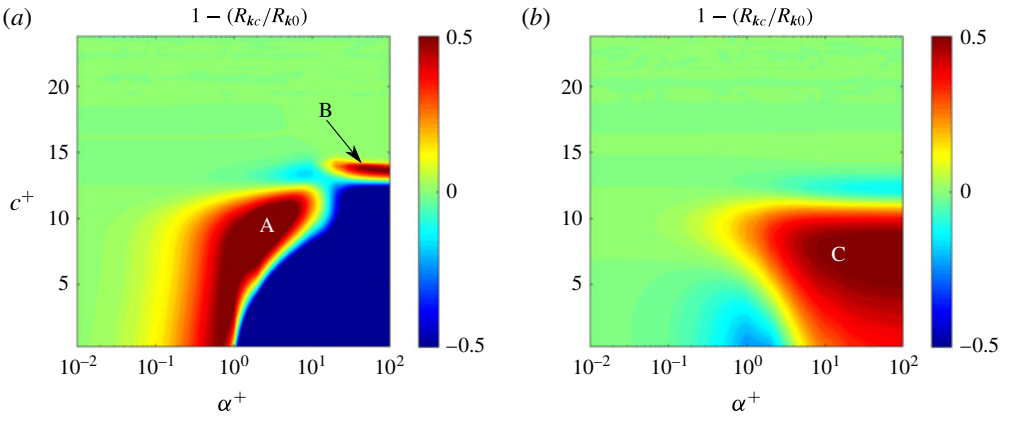

FIGURE 9. (Colour online) The normalized change in the Reynolds shear stress contribution relative to the uncontrolled case as a function of blowing and suction magnitude α^+ and propagation speed c^+ for resolvent modes with length scales comparable to the NW cycle at $Re_\tau = 2000$. (*a*) Case SP; (*b*) Case ST.

shows the normalized change of the Reynolds shear stress contribution relative to the uncontrolled case as a function of blowing and suction magnitude α^+, for modes with similar length scales as the near-wall cycle, $(\lambda_x^+, \lambda_z^+) \approx (10^3, 10^2)$, but different propagation speeds. Since the energetic contribution of structures with convection velocities larger than channel centreline U_{CL}^+ is known to be negligible in real turbulent flows, in the present study we focus on the modes with $0 < c^+ \leqslant U_{CL}^+$. For reference, the centreline velocity obtained using the eddy viscosity model proposed by Reynolds & Tiederman (1967) is $U_{CL}^+ = 23.8$ at $Re_\tau = 2000$.

For Case SP, figure 9(*a*) suggests that large drag reduction $(1 - (R_{kc}/R_{k0}) \approx 0.5)$ can be achieved at low magnitudes of blowing and suction for modes with low propagation speeds, especially in the ranges $6 \leqslant c^+ \leqslant 11$ and $1 \times 10^0 \leqslant \alpha^+ \leqslant 4 \times 10^0$ (A in the figure). In contrast, there is a significant increase in the Reynolds shear stress contribution from slower modes with $c^+ \leqslant 12$ when the blowing and suction magnitude becomes larger, $\alpha^+ \geqslant 10^1$. For the fast propagating modes ($c^+ \geqslant 15$), there is little or no control effect.

For Case ST, figure 9(*b*) shows an approximately 40 % drag reduction for slow propagating modes with $c^+ \leqslant 12$ when the blowing and suction magnitude is strong ($\alpha^+ \geqslant 10^1$; C in the figure), while drag increases for $\alpha^+ \leqslant 3 \times 10^0$ and $c^+ \leqslant 5$. In addition, modes with $c^+ \approx 12$–14 show drag increment over the entire range of blowing and suction magnitude studied in the present study. For even faster propagating modes with $c^+ \geqslant 15$, there is little or no control effect, similar to Case SP (figure 9*a*).

For this wavenumber–frequency combination, previous studies (McKeon & Sharma 2010; Luhar *et al.* 2014) classify slower-moving modes with $c^+ \leqslant 10$ as being 'attached' to the wall since the peak wall-normal velocity associated with these modes is located at a roughly fixed position ($20 \leqslant y^+ \leqslant 30$). On the other hand, as the propagation speed increases to $c^+ \geqslant 10$, the location of peak wall-normal velocity shifts away from the wall and tracks the critical layer, where $U^+(y_c^+) = c^+$. These faster-moving modes are termed 'critical' modes, and can be further classified into 'attached critical' or 'detached critical' depending on whether they have a substantial velocity signature in the near-wall region. Luhar *et al.* (2014) reported that wall-based

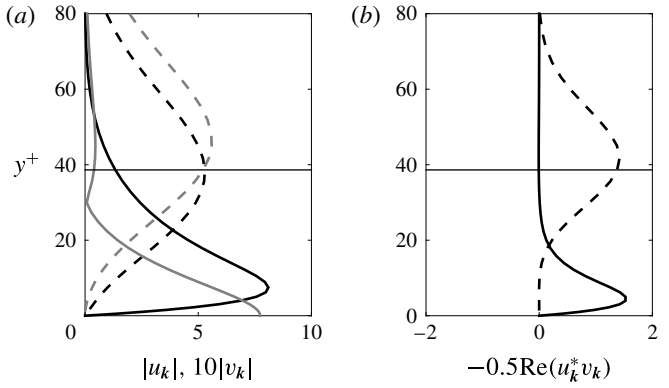

FIGURE 10. Wall-normal profiles for length scales comparable to the NW cycle with faster propagating speed $c^+ = 13.5$ at $Re_\tau = 2000$: (*a*) amplitude of streamwise velocity (black) and wall-normal velocity (grey); (*b*) Reynolds share stress. Dashed lines, no control; solid lines, Case SP at $\alpha^+ \approx 5 \times 10^1$. The horizontal dashed lines show the critical layer location, $y_c^+ \approx 39$.

control can be effective for attached modes but not necessarily for detached critical modes. Further, the transition region from attachment to criticality often tends to be harmful to control performance.

With these arguments in mind, the present results can be reviewed as follows. Suboptimal control has little effect on detached critical modes far from the wall ($c^+ \geqslant 15$), while strong effects (both good and harmful) can be seen for attached modes. In addition, similar to Luhar *et al.* (2014), the transition from attached to critical behaviour leads to a reversal in the control effect; sudden drag reduction (figure 8*a*) or temporary drag increment (figure 8*b*) is observed in the range of mode transition ($c^+ \approx 12$–15).

For modes with length scales comparable to the NW cycle, the present analysis shows that large Reynolds shear stress reductions are observed for $\alpha^+ \geqslant 3 \times 10^1$ and $c^+ \approx 13$–14 (B in figure 9*a*). However, the normalized change in singular values, $1 - (\sigma_{\boldsymbol{k}c}/\sigma_{\boldsymbol{k}0})^2$, shows further amplification in this region. In other words, the two measures used to evaluate control efficacy in this study show contradictory behaviour for this range of α^+ and c^+ (elsewhere, they are in good agreement). To provide further insight into this inconsistency, we consider how control under Case SP with $\alpha^+ = 50$ affects rank-1 mode structure for wavenumber–frequency combination $(\lambda_x^+, \lambda_z^+, c^+) \approx (10^3, 10^2, 13.5)$. Figure 10 shows that control leads to the development of a large near-wall peak in velocity and Reynolds stress ($y^+ < 10$), and a significant suppression around the critical layer, $y_c^+ \approx 39$. This observation suggests that, for region B, large-amplitude blowing and suction changes the structure of the rank-1 response mode completely compared to the uncontrolled case. Unlike the results shown in figure 4 for lower-amplitude blowing and suction, the rank-1 mode is not a modified version of the uncontrolled mode. Further, the first singular value under control is not significantly larger than subsequent singular values (i.e. $\sigma_{\boldsymbol{k}c,1}/\sigma_{\boldsymbol{k}c,3} \approx 1.4$, while $\sigma_{\boldsymbol{k}0,1}/\sigma_{\boldsymbol{k}0,3} \approx 4.1$). Thus, we suggest that for modes that are transitioning from being attached to detached, large values of α^+ weaken the rank-1 approximation, and trigger a 'new' kind of amplified flow structure close to the wall without influencing the original mode. The magnitude of α^+ that leads to effective suppression of NW modes is discussed further in § 4.1.1.

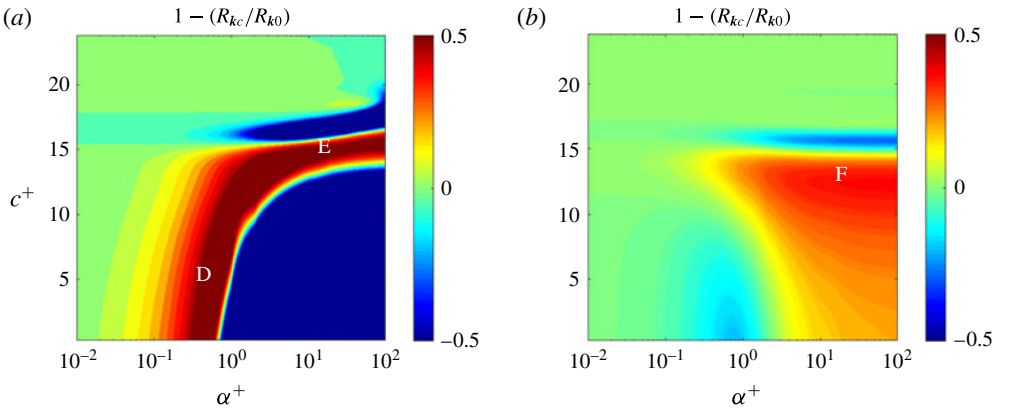

FIGURE 11. (Colour online) The normalized change in the Reynolds shear stress contribution relative to the uncontrolled case as a function of blowing and suction magnitude α^+ and propagation speed c^+ for modes with length scales similar to VLSMs at $Re_\tau = 2000$. (*a*) Case SP; (*b*) Case ST.

Figure 11 shows the normalized change of the Reynolds shear stress contribution for resolvent modes with similar length scales to the VLSMs, $(\lambda_x^+, \lambda_z^+) \approx (0.6h^+, 6h^+)$ at $Re_\tau = 2000$, for varying c^+ and α^+. For Case SP, figure 11(*a*) shows beneficial drag reduction is achieved at slow propagation speeds ($c^+ < 14$) for $10^{-1} \leqslant \alpha^+ \leqslant 10^0$ (D in the figure). As blowing and suction amplitude increases ($\alpha^+ \geqslant 2 \times 10^0$), a significant drag increment is observed. In contrast, for slightly higher speeds ($c^+ \approx 14$–16), drag reduction is observed over a wide range of blowing and suction magnitude, $\alpha^+ \geqslant 10^1$ (E in the figure). For critical modes with $16 \leqslant c^+ \leqslant 20$, significant drag increases are predicted over a wide range of blowing and suction magnitude.

A comparison of figures 9(*b*) and 11(*b*) shows that Case ST has a similar effect on both the VLSM- and NW-type modes. The major difference is that the preferable control effect (i.e. drag reduction) is observed over a wider range of propagation speeds: $c^+ \leqslant 15$ (F in figure 11*b*) compared to $c^+ \leqslant 12$ in figure 9(*b*). This difference is explained by the fact that modes with larger streamwise and spanwise length scales also tend to have a larger wall-normal footprint (Luhar *et al.* 2014). As a result, the transition from attachment to criticality occurs at a higher propagation speed: $c^+ \approx 15$ for modes with length scales similar to the VLSMs, compared to $c^+ \approx 12$ for modes with length scales comparable to the NW cycle.

3.4. *Effect of control in spectral space*

Up to here, we have discussed the effect of suboptimal control on modes resembling typical coherent structures in wall turbulence (§§ 3.1 and 3.2), considered the effect of phase speed c^+ (§ 3.3) and confirmed that control can lead to drag increment as well as reduction. Next, we consider the effect of control across wavenumber space. For a given wavenumber combination (k_x, k_z) corresponding to wavelength $(\lambda_x^+, \lambda_z^+)$, real turbulent flows are likely to involve many frequency components (i.e. many propagation speeds c). To account for this effect, we assume that the forcing for the resolvent operator is broadband over wave speed (Moarref *et al.* 2013). More specifically, we assume that there is unit forcing over the range of mode speeds $0 \leqslant c \leqslant 1$, where c is normalized by the centreline velocity, and predict the effect of

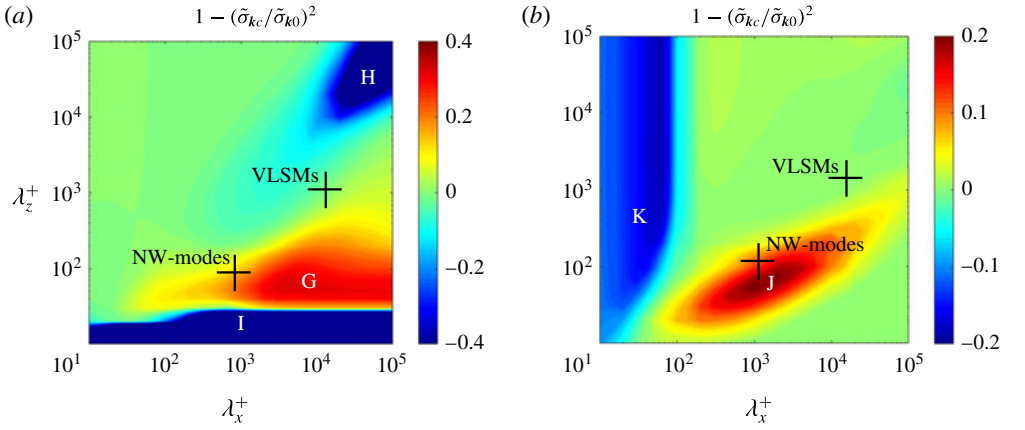

FIGURE 12. (Colour online) Normalized change of squared singular value relative to the uncontrolled case at $Re_\tau = 2000$: (*a*) Case SP ($\alpha^+ = 2.0$); (*b*) Case ST ($\alpha^+ = 10$).

control on modes with wavelengths in the range of $10^1 \leqslant (\lambda_x^+, \lambda_z^+) \leqslant 10^5$ by simply integrating squared singular values:

$$\tilde{\sigma}_{\boldsymbol{k}}^2(k_x, k_z) = \int_0^1 \sigma_{\boldsymbol{k}}^2(k_x, k_z, c)\,\mathrm{d}c. \tag{3.1}$$

Note that the broadband forcing assumption does not weight all frequency components equally. The resolvent operator itself acts as a strong filter on what frequency components, or mode speeds, are likely to be energetic in real turbulent flows. For example, only modes around $c^+ = 10$–18 are highly amplified (i.e. have high $\sigma_{\boldsymbol{k}}$) for modes with wavelength $\lambda_x^+ \approx 10^3$ and $\lambda_z^+ \approx 10^2$. The remaining frequency components do not contribute significantly to the integrated measure shown above.

Figure 12(*a*) shows the result for Case SP at $\alpha^+ = 2.0$ ($Re_\tau = 2000$). Consistent with the results presented above, the resolvent analysis predicts large drag reductions ($1 - (\tilde{\sigma}_{kc}/\tilde{\sigma}_{k0})^2 \geqslant 0.3$) for $\lambda_x^+ \geqslant 10^3$ and $\lambda_z^+ = 3 \times 10^1$–$3 \times 10^2$ (G in the figure), which is close to the wavenumber set of NW modes, i.e. $(\lambda_x^+, \lambda_z^+) \approx (10^3, 10^2)$. In contrast, a slight increase in drag is indicated in the spectral region representative of VLSMs (H in the figure). Further, the drag reduction effect deteriorates at shorter spanwise wavelength ($\lambda_z^+ < 3 \times 10^1$: I in the figure). Although not shown, we have also investigated the effect of Case SP with different blowing and suction magnitudes ($\alpha^+ = 0.5$, 1.0, 4.0 and 10). We have found that as the magnitude of blowing and suction increases, the region of drag reduction G diminishes, while the harmful region H widens. Region I, which represents drag increment, does not exist for $\alpha^+ = 0.5$. However, after this region appears, it becomes wider and wider as blowing and suction magnitude increases. In other words, the detrimental effects of suboptimal control at lower spanwise wavelengths increase as the blowing and suction magnitude α^+ increases above $\alpha^+ > 0.5$. These observations suggest that $\alpha^+ \approx 0.5$ represents a good design choice, since it yields some drag reduction for modes that resemble the NW cycle but avoids detrimental effects elsewhere in spectral space. Below, we show that the magnitude of blowing and suction employed in previous DNS (Lee *et al.* 1998) corresponds closely to this value.

Figure 12(*b*) shows the effect of control across spectral space for Case ST at $\alpha^+ = 10$ ($Re_\tau = 2000$). Substantial drag reduction ($1 - (\tilde{\sigma}_{kc}/\tilde{\sigma}_{k0})^2 \geqslant 0.2$) is indicated in

the region corresponding to NW modes (J in the figure). On the other hand, shorter streamwise wavelengths ($\lambda_x^+ < 10^2$) are adversely affected by the control (K in the figure). Unlike Case SP, as the magnitude of blowing and suction increases, the spectral region of drag increment (or drag reduction) does not significantly change in Case ST. However, the magnitude of the drag increment or reduction becomes larger. Note that, for modes with relatively long wavelengths (λ_x^+, $\lambda_z^+ > 10^3$), Case ST has almost no effect. In other words, Case ST is unlikely to affect modes resembling VLSMs.

In sum, the above results indicate that suboptimal control has a positive effect around the wavelengths of the NW modes for Case SP with $\alpha^+ = 2$ and Case ST with $\alpha^+ = 10$, but a detrimental (Case SP) or negligible (Case ST) effect around the wavelengths corresponding to VLSMs. At first glance, the fact that Case ST is predicted to have no detrimental effects on structures resembling VLSMs suggests that suboptimal control based on the streamwise shear stress may be useful for application at high Reynolds number. However, in the following section, we show that Case ST also leads to substantial amplification of structures that are long in the spanwise direction, which is detrimental to the overall performance of control.

4. Discussion

4.1. *Comparison with previous DNS studies*

In this section, we compare the present resolvent-based predictions with previous DNS studies (Lee *et al.* 1998; Choi & Sung 2002; Iwamoto *et al.* 2002). To provide further insight into the difference between Case SP and Case ST, we also conduct additional channel flow DNS using an in-house code (Fukagata, Kasagi & Koumoutsakos 2006) for representative values of α^+. Briefly, these simulations have following key properties: the code is based on energy conservative finite difference method for the channel flow; the time integration is done by using the third-order Runge–Kutta/Crank–Nicolson scheme; the bulk mean velocity is kept constant and the friction Reynolds number is $Re_\tau \approx 180$ for uncontrolled flow; the computational domain is $(L_x, L_y, L_z) \approx (7, 2, 3.5)$; finally, grid number dependencies for the time scale and spatial space have been well verified.

4.1.1. *Case SP*

For a fair comparison between the present predictions and the DNS results, the parameter α^+ should be related to the blowing and suction amplitudes used in the DNS. In the DNS studies, the root-mean-square value of the control input ϕ_{rms}^+ was kept constant, at a value corresponding to the wall-normal velocity at $y^+ \approx 10$. In contrast, the present analysis considers α^+ to be a design parameter.

As a first step, we estimate a realistic value for the magnitude α^+ for Case SP based on values of ϕ_{rms}^+ from previous DNS studies. As mentioned in § 2.2, suboptimal control aims to suppress the quasi-streamwise vortices associated NW cycle (this is generally true for most active control techniques). For the relative long modes resembling the NW cycle, the streamwise wavenumber is an order of magnitude smaller than the spanwise wavenumber, $k_x \ll k_z$, such that $k_z/K \approx 1$ (Lee *et al.* 1998). For example, $k_z/K = 120/\sqrt{12^2 + 120^2} \approx 0.995$ for NW modes at $Re_\tau = 2000$ in the analysis employed here. Assuming $k_z/K \approx 1$ in (2.15), we can derive the following relationship between the amplitudes of the control input and the spanwise wall shear stress:

$$\left|\phi_{\boldsymbol{k}}^+\right| \simeq \alpha^+ \left|\left(\partial w_{\boldsymbol{k}}^+/\partial y^+\right)_w\right|. \tag{4.1}$$

Reference	Re_τ	R.m.s. of the control input (Case SP)
Lee *et al.* (1998)	110	$\phi^+_{rms} \approx 0.155$
Iwamoto *et al.* (2002)	110–650	$\phi^+_{rms} \approx 0.075$–$0.125$
Choi & Sung (2002)	100	$\phi^+_{rms} \approx 0.125$(optimum)–$0.3$

TABLE 1. The information of root-mean-square values from previous DNS studies.

Thus, the magnitude of α^+ can be estimated from ϕ^+_{rms} and $\left(\partial w^+_{rms}/\partial y^+\right)_w$ obtained in DNS. Based on results from the in-house DNS at $Re_\tau = 180$ (Fukagata *et al.* 2006), the magnitude of the spanwise wall shear stress is estimated to be

$$\left(\partial w^+_{rms}/\partial y^+\right)_w \approx 0.2, \tag{4.2}$$

although any database of turbulent channel flow at similar low Reynolds numbers should yield similar values. As shown in table 1, the blowing and suction amplitude used in the DNS studies (Lee *et al.* 1998; Choi & Sung 2002; Iwamoto *et al.* 2002) is

$$\phi^+_{rms} \approx 0.1. \tag{4.3}$$

Combining these two estimates, α^+ for Case SP in the DNS studies is approximately

$$\alpha^+ \approx \frac{\phi^+_{rms}}{\left(\partial w^+_{rms}/\partial y^+\right)_w} \approx \frac{0.1}{0.2} = 0.5. \tag{4.4}$$

The full range of ϕ^+_{rms} employed in previous DNS (0.075–0.3) yields $\alpha^+ \approx 0.375$–1.5. As discussed in § 3.4, this range of α^+ corresponds closely to the qualitative optimum where the NW modes are suppressed due to the blowing and suction, but the damaging effects elsewhere in spectral space are limited. Further, figure 3(*b*) indicates that the Reynolds stress contribution from the NW modes is suppressed by approximately 25 % for Case SP with $\alpha^+ \approx 0.5$. This is in good agreement with the 22 % drag reduction obtained by Lee *et al.* (1998). These observations suggest that $\alpha^+ \approx 0.5$ represents a reasonable estimate for the conditions tested in previous DNS, and that the resolvent analysis is able to successfully reproduce the effects of suboptimal control based on the spanwise shear stress.

Since the r.m.s. value of ϕ was set to equal that of the wall-normal velocity at $y^+ \approx 10$ in the original DNS of Lee *et al.* (1998), as another quantitative comparison, we attempt to find the value of α^+ that leads to $|\phi_k| = |v_k(y^+ = 10)|$ for the NW modes. As shown in figure 13(*a*), $|\phi_k| = |v_k(y^+ \approx 10)|$ when $\alpha^+ = 1.0$. This observation confirms that $\alpha^+ \approx 0.5$–1.0 represents a reasonable estimate for the conditions tested in DNS. Importantly, an estimate for α^+ also allows us to compare Case SP with the opposition control of Choi *et al.* (1994). Figure 13(*b*) shows that there are many similarities between Case SP with $\alpha^+ = 1.0$ and opposition control with the detection plane at $y^+_d \approx 10$. The phase of wall-normal velocity is reversed between $y^+ = 10$ and the wall for both Case SP and the opposition control. Namely, ϕ_k and $v_k(y^+ = 10)$ have opposite signs. These features have also been confirmed in figure 5(*c*,*d*) (Case SP, $\alpha^+ \approx 2.0$). The trajectory of the phase from $y^+ = 10$ to the wall, however, is somewhat different: for the opposition control, the phase decreases towards the wall, while it increases in Case SP. Figure 13(*b*) also shows that the phase angle between

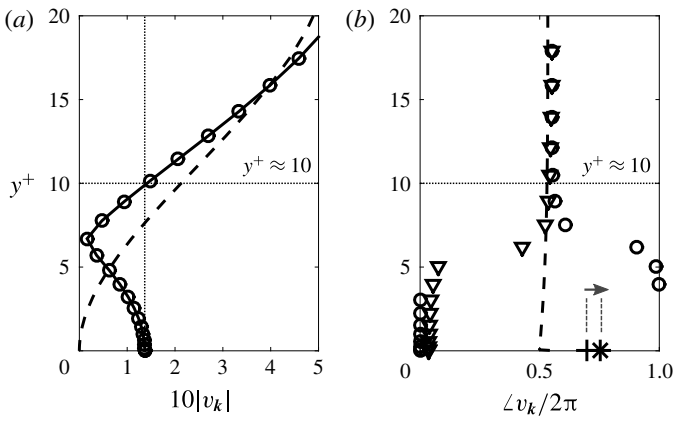

FIGURE 13. Profiles showing wall-normal variations in structure for resolvent modes: (*a*) amplitude $|v_k|$ and (*b*) phase $\angle v_k$ of wall-normal velocity. Dashed lines, uncontrolled; circle markers, Case SP ($\alpha^+ = 1.0$); triangle markers, opposition control ($y_d^+ \approx 10$). In (*b*), phase of spanwise wall shear stress is also shown: cross, $(\partial w_{k0}/\partial y)_w$; asterisk, $(\partial w_{kc}/\partial y)_w$. Each figure considers NW modes at $Re_\tau = 2000$.

the spanwise wall shear stress and the control input is about $\pi/2$, although a slight phase shift is observed from the uncontrolled to controlled, as highlighted by the arrow annotation. In summary, Case SP can essentially be regarded as a modified version of opposition control. We will further compare the resolvent-based predictions of suboptimal control and opposition control in § 4.2.

4.1.2. *Case ST*

Next, we consider the discrepancy for Case ST between the present study and the previous DNS. Recall that Lee *et al.* (1998) observed an increase in drag for Case ST, while the resolvent-based predictions shown in figure 3 indicate drag reduction. In addition, figures 9(*b*) and 11(*b*) indicate that Case ST has positive effects around the wavelengths of both NW modes and VLSMs when we consider modes that are attached (i.e. slow propagating modes).

The key to explaining the discrepancy between DNS and the present analysis for Case ST is the rise of flow structures that are detrimental to control performance. As shown in figure 12(*b*), resolvent analysis suggests that quasi-two-dimensional structures that are long in the spanwise direction, with streamwise wavelength $\lambda_x^+ \approx 10^2$ (region K), are amplified substantially under control. To test whether such structures emerge in real flows, we conducted DNS using the in-house code mentioned earlier (Fukagata *et al.* 2006). Figure 14 shows contours of the control input (i.e. the blowing and suction) at the lower wall for Case SP with $\alpha^+ \approx 1$ and for Case ST with $\alpha^+ \approx 5$. Here, the control input is computed using the uncontrolled velocity field, which corresponds to the control input at the initial time instant when the control is applied. For Case SP (figure 14*a*), the velocity contours are long in the streamwise direction and exhibit alternating regions of positive velocity (i.e. blowing) and negative velocity (i.e. suction) in the spanwise direction. These qualitative observations confirm that Case SP targets the quasi-streamwise vortices associated with the NW cycle. On the other hand, for Case ST (figure 14*b*), the blowing and

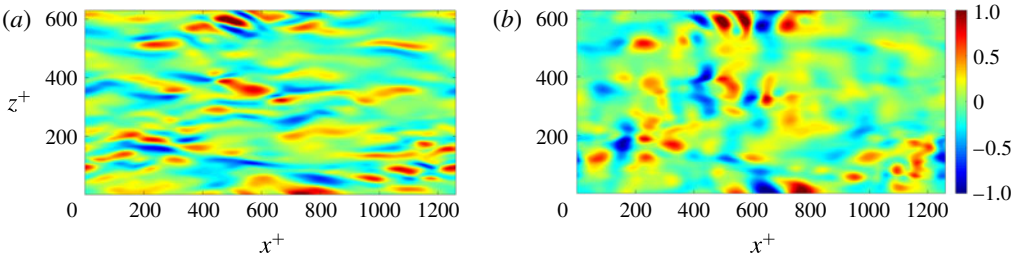

FIGURE 14. (Colour online) Contours show the snapshot of the control input ϕ^+ at the lower wall calculated by in-house DNS code ($Re_\tau = 180$): (*a*) Case SP; (*b*) Case ST.

suction contours are more elongated in the spanwise direction and much shorter in the streamwise direction. In other words, the control input does not appear to be targeting or interacting with the NW cycle. Snapshots taken at regular intervals show that these quasi-two-dimensional structures that are long in the spanwise direction persist under control based on the streamwise velocity.

As an additional quantitative test, we also generated wavenumber spectra for the control input (for 1000 snapshots acquired at intervals of $t^+ \approx 100$). Note that the distributions of control input, used for the time-average operation, are computed from different snapshots of uncontrolled (i.e. no-slip condition) DNS field. These spectra (not shown here) indicated the presence of an energetic peak in the range of $\lambda_x^+ \approx 1.5 \times 10^2 - 4 \times 10^2$ and $\lambda_z^+ \approx 3 \times 10^2 - 6 \times 10^2$ for Case ST. In contrast, there was a peak near length scales corresponding closely to the NW cycle for Case SP, i.e. $(\lambda_x^+, \lambda_z^+) \approx (10^3, 10^2)$. The length scales for the structures that are highly actuated initially under Case ST do not correspond exactly to the region of highest amplification (K) in figure 12(*b*). However, these results suggest that streamwise shear-based control sets up a detrimental feedback loop whereby the actuation preferentially targets structures that are short in the streamwise direction and long in the spanwise direction (i.e. high k_x/k_z), which corresponds to the region of spectral space that exhibits very high amplification under control.

In summary, while suboptimal control based on the streamwise velocity (Case ST) may suppress the NW cycle, it also leads to the emergence of energetic structures that are long in the spanwise direction. Such energetic spanwise structures could be responsible for the drag increase reported in previous studies (Lee *et al.* 1998). Further, the present study suggests that it may be possible to reduce drag under Case ST if the control is applied selectively in spectral space. Specifically, actuation must be limited to regions of spectral space where the resolvent analysis predicts a reduction in gain or Reynolds stress (e.g. for wavenumber–frequency combinations corresponding to the near-wall cycle, as shown in figures 9(*b*) and 12(*b*)). Further simulations that test this hypothesis are currently underway.

4.1.3. *Interpretation of Reynolds number effect*

Finally, we consider the deterioration of control effect at high Reynolds numbers. Iwamoto *et al.* (2002) investigated the effect of suboptimal control (Case SP) at several friction Reynolds numbers ($Re_\tau = 110,\ 150,\ 300,\ 400$ and 650) and reported that the drag reduction rate decreases with increasing Re_τ. Assuming that the near-wall velocity fluctuations are ideally damped, Iwamoto *et al.* (2005) also derived a theoretical expression capturing the Reynolds number dependence of the drag

reduction rate. According to this theory, the drag reduction rate mildly decreases with the Reynolds number even if the large-scale structures are not taken into account. As we have observed in figure 3, the Reynolds number has little influence on the singular values and the Reynolds shear stress contributions for NW modes in the range where the drag is predicted to decrease, i.e. $10^0 \leqslant \alpha^+ \leqslant 5 \times 10^0$. On the other hand, as illustrated in figure 6, the singular value ratios and Reynolds stress contributions for VLSMs in the same range of α^+ indicate drag increase. Therefore, the deterioration of control at high Reynolds numbers is likely due to a combination of the fundamental Reynolds number effect considered by Iwamoto *et al.* (2005) and the detrimental effect of control on longer wavelength structures.

4.2. *Comparison with the opposition control*

Here, we compare resolvent-based predictions for suboptimal control and opposition control in turbulent channel flow, focusing on modes resembling the NW cycle at $Re_\tau = 2000$. As mentioned previously, the suboptimal control of Lee *et al.* (1998) stems from the opposition control of Choi *et al.* (1994). Previous DNS and LES studies of opposition-controlled channel and pipe flows (Hammond, Bewley & Moin 1998; Chang, Collis & Ramakrishnan 2002; Fukagata & Kasagi 2003) report that maximum drag reduction is achieved when the detection plane is located at $y_d^+ \approx 15$, and drag increases significantly above $y_d^+ > 25$. This trend was successfully reproduced by Luhar *et al.* (2014) for a turbulent pipe flow.

In the present study, we have also performed resolvent analyses of opposition-controlled channel flow. Although the results are not reproduced here for brevity, these analyses show that opposition control for NW modes achieves significant suppression of R_k near $y_d^+ \approx 20$. Consistent with the pipe flow predictions of Luhar *et al.* (2014), the drag contribution (σ_k) is minimized at $y_d^+ \approx 16$. We also observe that the drag contribution from VLSMs increases under opposition control, regardless of the detection plane location. Hereafter, we focus on the opposition control for NW-type modes with $y_d^+ \approx 16$ and $y_d^+ \approx 20$ in order to compare with the results obtained for suboptimal control. Note that $y_d^+ \approx 16$ corresponds to the case where the detection plane and the critical layer are co-located.

Figure 15 shows profiles of velocity amplitude and Reynolds shear stress for both suboptimal and opposition control. The blowing and suction magnitude is set at $\alpha^+ = 2.0$ for suboptimal control (Case SP), while the detection plane for opposition control is assumed to be $y_d^+ \approx 16$. These profiles show substantial similarities between the two control methods. Further, the present results for opposition control (circle markers) are very similar to the those of pipe flow (Luhar *et al.* 2014).

Figure 16 compares the predictions for Case SP at $\alpha^+ = 4.0$, which maximizes suppression of the Reynolds shear stress contribution, with predictions for opposition control with $y_d^+ \approx 20$. The streamwise velocity profiles are quite similar for both controlled cases, particularly near the wall. However, the wall-normal velocity above the critical layer shows some important differences; $|v_k|$ is slightly reduced under suboptimal control but enhanced under opposition control (figure 16*b*). Interestingly, despite the significant suppression of Reynolds shear stress, figure 16(*a*) shows that the peak location of controlled streamwise velocity moves between the critical layer and the wall for Case SP with $\alpha^+ = 4.0$. This is in contrast to the results shown in figure 15(*a*) for $\alpha^+ = 2.0$. Luhar *et al.* (2014) reported that the displacement of peak of $|u_k|$ away from the critical layer may weaken the critical layer mechanism.

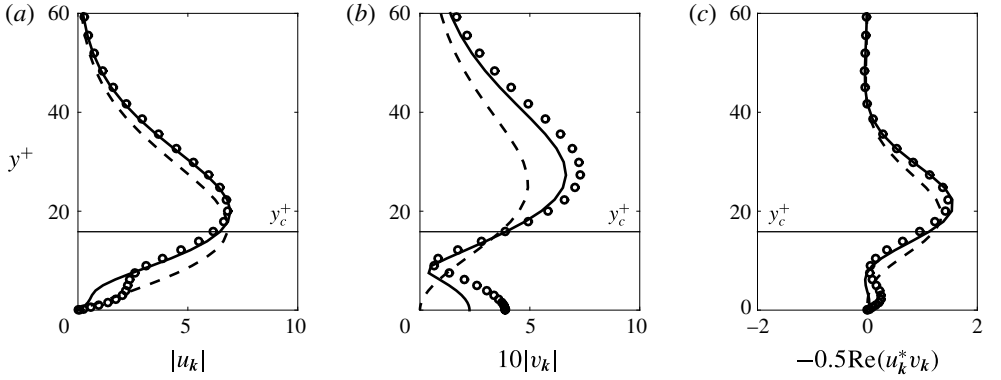

FIGURE 15. Wall-normal profiles for modes resembling the NW cycle at $Re_\tau = 2000$: (*a*) amplitude of streamwise velocity; (*b*) amplitude of wall-normal velocity; (*c*) Reynolds shear stress. Dashed lines, uncontrolled; solid line, suboptimal control ($\alpha^+ = 2.0$); circle marker, opposition control ($y_d^+ \approx 16$). The solid horizontal lines indicate the critical layer location y_c^+. The detection plane is located at the same y value as the critical layer.

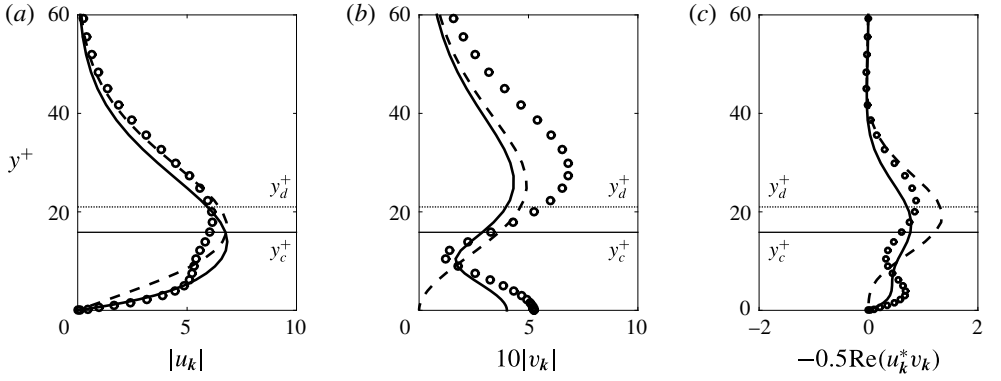

FIGURE 16. Wall-normal profiles for modes resembling the NW cycle at $Re_\tau = 2000$: (*a*) amplitude of streamwise velocity; (*b*) amplitude of wall-normal velocity; (*c*) Reynolds shear stress. Dashed lines, uncontrolled; solid line, suboptimal control ($\alpha^+ = 4.0$); circle marker, opposition control ($y_d^+ \approx 20$). The solid horizontal lines show the critical layer location y_c^+. The dashed horizontal lines indicate the detection plane location for opposition control.

Now, we define a new measure which focuses only on the Reynolds stress contribution in the region between the wall and the critical layer:

$$R_{k,attached} = \int_{-1}^{-1+y_c} \sigma_k^2 \ \mathrm{Re}(u_k{}^* v_k)(+y)\,\mathrm{d}y + \int_{1-y_c}^{1} \sigma_k^2 \ \mathrm{Re}(u_k{}^* v_k)(+y)\,\mathrm{d}y. \qquad (4.5)$$

Here, the first term in (4.5) considers the region attached to the lower wall and the second term considers the region close to the upper wall. As shown in rightmost column of table 2, this near-wall Reynolds shear stress contribution exhibits different trends compared to the total contribution. $R_{k,attached}$ is strongly suppressed for Case SP at $\alpha^+ = 2.0$ and for opposition control with $y_d^+ \approx 16$. However, for Case SP with $\alpha^+ = 4.0$ and the opposition control with $y_d^+ \approx 20$, the ratios are recovered toward unity.

Control method	y_d^+	α^+	σ_{kc}/σ_{k0}	R_{kc}/R_{k0}	$(R_{kc}/R_{k0})_{attached}$
Opposition	16	—	0.55	0.32	0.19
Suboptimal	—	2.0	0.61	0.40	0.23
Opposition	20	—	0.54	0.23	0.29
Suboptimal	—	4.0	0.72	0.35	0.54

TABLE 2. The ratio of controlled to uncontrolled σ_k and R_k for each control method.

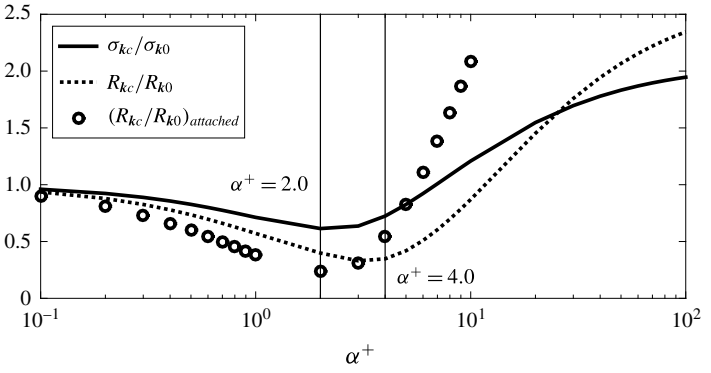

FIGURE 17. Evaluating the turbulent drag contribution in different ways. Case SP at $Re_\tau = 2000$ (NW modes).

Figure 17 shows $(R_{kc}/R_{k0})_{attached}$ as a function of blowing and suction magnitude α^+, which helps further clarify the drag reduction mechanism for NW modes under suboptimal control based on spanwise wall shear stress (Case SP). The slope is negative (i.e. towards reduced drag contribution) up to $\alpha^+ = 2.0$ and positive (i.e. towards increased drag contribution) above this value. The channel-integrated Reynolds shear stress contribution R_k still decreases between $2.0 \leqslant \alpha^+ \leqslant 4.0$. However, the Reynolds shear stress contribution in the near-wall region $R_{k,attached}$ begins to increase at that point.

Further explanation is provided in figure 18. The peak location of controlled streamwise velocity shifts up above the critical layer up to $\alpha^+ = 2.0$. For larger α^+, the peak in streamwise velocity shifts downwards and localizes between the critical layer and the wall when blowing and suction magnitude is $\alpha^+ \geqslant 3.0$. In addition, the peak value of wall-normal velocity is larger than that for the uncontrolled case in the range of $\alpha^+ \leqslant 2.0$, while smaller in the range $\alpha^+ \geqslant 3.5$. These trends confirm that, beyond a certain threshold, an increase in the magnitude of blowing and suction only serves to generate additional turbulence near the wall. This increase in near-wall velocities with increasing α^+ is also evident in figure 5(*e*,*f*).

In summary, σ_{kc}/σ_{k0} and $R_{k,attached}$ are minimized for $\alpha^+ = 2.0$, which resembles opposition control with $y_d^+ \approx 16$. The channel-integrated Reynolds shear stress contribution R_k is minimized at a slightly larger value of α^+ due to the suppression above the critical layer.

5. Conclusions

Following previous studies (Luhar *et al.* 2014, 2015, 2016), the results presented above show that the resolvent formulation has the potential to serve as a powerful

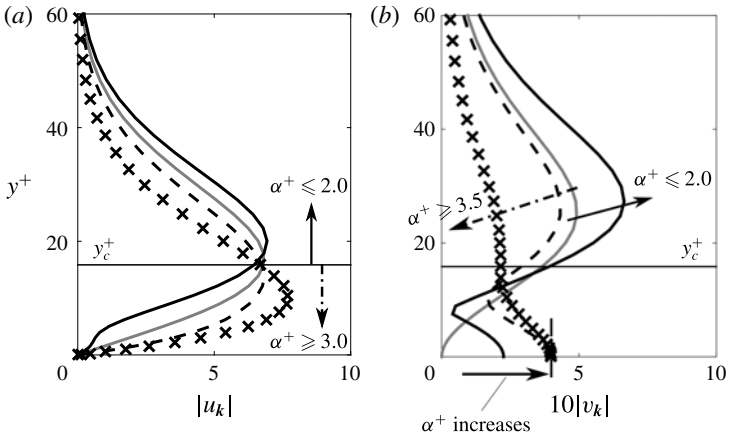

FIGURE 18. Wall-normal profiles for modes resembling the NW cycle at $Re_\tau = 2000$ for varying blowing and suction magnitudes (Case SP): Grey, uncontrolled; solid lines, $\alpha^+ = 2.0$; dashed lines, $\alpha^+ = 4.0$; cross markers, $\alpha^+ = 10^3$. The arrows indicate the directions of velocity components movements, which depend on blowing and suction magnitude.

predictive tool for the design and evaluation of (linear) control laws for wall-bounded turbulent flows. In addition, the formulation also provides fundamental physical insights into the effects of control on dynamically important features of wall turbulence.

For the suboptimal control laws proposed by Lee *et al.* (1998), resolvent analysis predicts that the effect of control across spectral space depends strongly on whether the streamwise shear (Case ST) or spanwise shear (Case SP) is used as the control input. Relative to the uncontrolled flow, Case SP suppresses modes resembling the NW cycle and further amplifies modes resembling the VLSMs when the blowing and suction parameter ranges from $1 \leqslant \alpha^+ \leqslant 5$. As the blowing and suction magnitude increases such that $\alpha^+ \geqslant 10$, the effects of control on these structures are reversed. For Case ST, the analysis predicts that NW-modes are suppressed across all α^+, while modes resembling the VLSMs are further amplified. However, the maximum suppression possible for the NW modes is lower under Case ST compared to Case SP, and requires larger α^+. In other words, Case SP leads to a larger reduction in gain, and for less intense actuation. An increase in Reynolds number from $Re_\tau = 110$ to $Re_\tau = 2000$ does not appreciably change the above trends.

We also investigated the effects of mode speed on control efficacy (§ 3.3). Consistent with previous resolvent-based predictions for opposition control (Luhar *et al.* 2014), suboptimal control has the largest effect on slower-moving modes that are localized closer to the wall (i.e. attached modes). The gain and structure of faster-moving modes (i.e. critical or detached modes) found farther from the wall do not change significantly under control. Physically, this can be explained as following: faster-moving detached modes do not have an appreciable signature at the wall, and so any control technique that employs wall-based sensing and actuation cannot interact such modes. Importantly, note that attached large-scale structures such as VLSMs do interact with and influence the NW region (Marusic *et al.* 2010). As a result, it may be possible to design wall-based control that suppresses such structures. There are also close similarities between the mode structures predicted for opposition control

and for suboptimal control based on spanwise shear. In particular, the predicted mode structures suggest that suboptimal control is essentially a modified version of opposition control (Choi *et al.* 1994), with a phase lag that depends on mode speed and the magnitude of blowing and suction (i.e. the design parameter α^+).

In addition to considering the gain and structure for individual modes resembling the NW cycle and VLSMs, we also compared the effect of suboptimal control across spectral space. Both Case SP and Case ST favourably affect (i.e. suppress) structures with length scales comparable to the NW cycle. Case SP is predicted to detrimentally affect (i.e. further amplify) structures with length scales comparable to the VLSMs, while Case ST is predicted to have little or no effect on these larger structures. For Case SP, control performance is very sensitive to the magnitude of blowing and suction. As α^+ increases, the spectral region over which modes are suppressed diminishes, while the region over which modes are further amplified widens.

To allow for a quantitative comparison between resolvent-based predictions and previous DNS, we estimated the design parameter α^+ from previous databases. Specifically, a comparison of r.m.s. values for the turbulent spanwise shear and the wall-based blowing and suction suggests that $\alpha^+ \approx 0.5$–1.0 in previous DNS for suboptimal control (Lee *et al.* 1998; Choi & Sung 2002; Iwamoto *et al.* 2002). For this range of α^+, resolvent analysis suggests that Case SP reduces the Reynolds shear stress contribution from NW modes by approximately 25 %, which is consistent with the 22 % reduction in drag observed in DNS.

For Case ST, resolvent analysis predicts that control leads to a small, but meaningful, reduction in gain for modes resembling the NW cycle. However, Lee *et al.* (1998) observed an increase in drag in their DNS. The results presented in § 4.1.2 provide a clear explanation for this discrepancy. Specifically, resolvent analysis reveals that Case ST can lead to a substantial increase in amplification for structures that are relatively long in the spanwise direction. High actuation of such energetic spanwise structures was confirmed in a limited DNS investigation at $Re_\tau \approx 180$, both via instantaneous snapshots of the flow field and time-averaged statistics.

Finally, we developed a new measure which focuses only on the Reynolds stress contribution very close to the wall, $R_{\boldsymbol{k},attached}$. This measure provides insight into why the resolvent analysis occasionally yields differing predictions for changes in gain ($\sigma_{\boldsymbol{k}c}/\sigma_{\boldsymbol{k}0}$) and the Reynolds shear stress contribution ($R_{\boldsymbol{k}c}/R_{\boldsymbol{k}0}$) due to control.

Acknowledgement

The authors are grateful to Dr J. Kim (UCLA) and Dr B. J. McKeon (Caltech) for sowing a seed for this collaborative work at IPAM Workshop on Mathematics of Turbulence, Workshop IV: Turbulence in Engineering Applications, UCLA, CA, USA, November 17–21, 2014. S.N. and K.F. are also grateful to Drs S. Obi and K. Ando (Keio University) and Dr H. Mamori (Tokyo University of Science) for fruitful discussion. This work was supported through Grant-in-Aid for Scientific Research (C) (no. 25420129) by Japan Society for the Promotion of Science (JSPS). This material is based upon work supported by the Air Force Office of Scientific Research under award number FA9550-17-1-0142 (M.L.).

REFERENCES

ABDULBARI, H. A., YUNUS, R. M., ABDURAHMAN, N. H. & CHARLES, A. 2013 Going against the flow – a review of non-additive means of drag reduction. *J. Ind. Engng Chem.* **19**, 27–36.

ADRIAN, R. J. 2007 Hairpin vortex organization in wall turbulence. *Phys. Fluids* **19**, 041301.

CHANG, Y., COLLIS, S. S. & RAMAKRISHNAN, S. 2002 Viscous effects in control of near-wall turbulence. *Phys. Fluids* **14**, 4069–4080.

CHERNYSHENKO, S. I. & BAIG, M. F. 2005 The mechanism of streak formation in near-wall turbulence. *J. Fluid Mech.* **544**, 99–131.

CHOI, H., MOIN, P. & KIM, J. 1994 Active turbulence control for drag reduction in wall-bounded flows. *J. Fluid Mech.* **262**, 75–110.

CHOI, J.-I. & SUNG, H. J. 2002 Assessment of suboptimal control for drag reduction in turbulent channel flow. *J. Turbul.* **3** (29), 1–17.

CHUNG, Y. M. & TALHA, T. 2011 Effectiveness of active flow control for turbulent skin friction drag reduction. *Phys. Fluids* **23**, 025102.

FUKAGATA, K., IWAMOTO, K. & KASAGI, N. 2002 Contribution of Reynolds stress distribution to the skin friction in wall-bounded flows. *Phys. Fluids* **14**, L73–L76.

FUKAGATA, K. & KASAGI, N. 2003 Drag reduction in turbulent pipe flow with feedback control applied partially to wall. *Intl J. Heat Fluid Flow* **24**, 480–490.

FUKAGATA, K. & KASAGI, N. 2004 Suboptimal control for drag reduction via suppression of near-wall Reynolds shear stress. *Intl J. Heat Fluid Flow* **25**, 341–350.

FUKAGATA, K., KASAGI, N. & KOUMOUTSAKOS, P. 2006 A theoretical prediction of friction drag reduction in turbulent flow by superhydrophobic surfaces. *Phys. Fluids* **18**, 051703.

GAD-EL-HAK, M. 1994 Interactive control of turbulent boundary layers-a futuristic overview. *AIAA J.* **32**, 1753–1765.

GAD-EL-HAK, M. 2000 *Flow Control: Passive, Active, and Reactive Flow Management*. Cambridge University Press.

HAMILTON, J. M., KIM, J. & WALEFFE, F. 1995 Regeneration mechanisms of near-wall turbulence structures. *J. Fluid Mech.* **287**, 317–348.

HAMMOND, E. P., BEWLEY, T. R. & MOIN, P. 1998 Observed mechanisms for turbulence attenuation and enhancement in opposition controlled wall-bounded flows. *Phys. Fluids* **10**, 2421–2423.

HOEPFFNER, J. & FUKAGATA, K. 2009 Pumping or drag reduction? *J. Fluid Mech.* **635**, 171–187.

HUTCHINS, N. & MARUSIC, I. 2007*a* Evidence of very long meandering features in the logarithmic region of turbulent boundary layers. *J. Fluid Mech.* **579**, 1–28.

HUTCHINS, N. & MARUSIC, I. 2007*b* Large-scale influences in near-wall turbulence. *Phil. Trans. R. Soc.* A **365**, 647–664.

IWAMOTO, K., FUKAGATA, K., KASAGI, N. & SUZUKI, Y. 2005 Friction drag reduction achievable by near-wall turbulence manipulation at high Reynolds numbers. *Phys. Fluids* **17**, 011702.

IWAMOTO, K., SUZUKI, Y. & KASAGI, N. 2002 Reynolds number effect on wall turbulence: toward effective feedback control. *Intl J. Heat Fluid Flow* **23**, 678–689.

KARNIADAKIS, G. E. & CHOI, K.-S. 2003 Mechanisms on transverse motions in turbulent wall flows. *Annu. Rev. Fluid Mech.* **35**, 45–62.

KASAGI, N., SUZUKI, Y. & FUKAGATA, K. 2009 Microelectromechanical systems-based feedback control of turbulence for skin friction reduction. *Annu. Rev. Fluid Mech.* **41**, 231–251.

KAWAHARA, G. & KIDA, S. 2001 Periodic motion embedded in plane Couette turbulence: regeneration cycle and burst. *J. Fluid Mech.* **449**, 291–300.

KIM, J. 2003 Control of turbulent boundary layers. *Phys. Fluids* **15**, 1093–1105.

KIM, J. & LIM, J. 2000 A linear process in wall-bounded turbulent shear flows. *Phys. Fluids* **12**, 1885–1888.

KIM, J., MOIN, P. & MOSER, R. 1987 Turbulence statistics in fully-developed channel flow at low Reynolds-number. *J. Fluid Mech.* **177**, 133–166.

KLINE, S. J., REYNOLDS, W. C., SCHRAUB, F. A. & RUNSTADL, P. W. 1967 Structure of turbulent boundary layers. *J. Fluid Mech.* **30**, 741–773.

LEE, C., KIM, J. & CHOI, H. 1998 Suboptimal control of turbulent channel flow for drag reduction. *J. Fluid Mech.* **358**, 245–258.

LIEU, B. K., MOARREF, R. & JOVANOVIĆ, M. R. 2010 Controlling the onset of turbulence by streamwise travelling waves. Part 2. Direct numerical simulation. *J. Fluid Mech.* **663**, 100–119.

LIM, J. & KIM, J. 2004 A singular value analysis of boundary layer control. *Phys. Fluids* **16**, 1980–1988.

LUHAR, M., SHARMA, A. S. & MCKEON, B. J. 2014 Opposition control within the resolvent analysis framework. *J. Fluid Mech.* **749**, 597–626.

LUHAR, M., SHARMA, A. S. & MCKEON, B. J. 2015 A framework for studying the effect of compliant surfaces on wall turbulence. *J. Fluid Mech.* **768**, 415–441.

LUHAR, M., SHARMA, A. S. & MCKEON, B. J. 2016 On the design of optimal compliant walls for turbulence control. *J. Turbul.* **17**, 787–806.

MAMORI, H., IWAMOTO, K. & MURATA, A. 2014 Effect of the parameters of traveling waves created by blowing and suction on the relaminarization phenomena in fully developed turbulent channel flow. *Phys. Fluids* **26**, 015101.

MAMORI, H., FUKAGATA, K. & HOEPFFNER, J. 2010 Phase relationship in laminar channel flow controlled by traveling-wave-like blowing or suction. *Phys. Rev.* E **81**, 046304.

MARUSIC, I., MATHIS, R. & HUTCHINS, N. 2010 Predictive model for wall-bounded turbulent flow. *Science* **329** (5988), 193–196.

MCKEON, B. J., JACOBI, I. & SHARMA, A. S. 2013 Experimental manipulation of wall turbulence: a systems approach. *Phys. Fluids* **25**, 031301.

MCKEON, B. J. & SHARMA, A. S. 2010 A critical-layer framework for turbulent pipe flow. *J. Fluid Mech.* **658**, 336–382.

MIN, T., KANG, S. M., SPEYER, J. L. & KIM, J. 2006 Sustained sub-laminar drag in a fully-developed channel flow. *J. Fluid Mech.* **558**, 309–318.

MOARREF, R. & JOVANOVIĆ, M. R. 2010 Controlling the onset of turbulence by streamwise travelling waves. Part 1. Receptivity analysis. *J. Fluid Mech.* **663**, 70–99.

MOARREF, R., SHARMA, A. S., TROPP, J. A. & MCKEON, B. J. 2013 Model-based scaling and prediction of the streamwise energy intensity in high-Reynolds number turbulent channels. *J. Fluid Mech.* **734**, 275–316.

MONTY, J. P., HUTCHINS, N., NG, H. C. H., MARUSIC, I. & CHONG, M. S. 2009 A comparison of turbulent pipe, channel and boundary layer flows. *J. Fluid Mech.* **632**, 431–442.

NAKANISHI, R., MAMORI, H. & FUKAGATA, K. 2012 Relaminarization of turbulent channel flow using traveling wave-like wall deformation. *Intl J. Heat Fluid Flow* **35**, 152–159.

QUADRIO, M. 2011 Drag reduction in turbulent boundary layers by in-plane wall motion. *Phil. Trans. R. Soc. Lond.* A **369**, 1428–1442.

REYNOLDS, W. C. & TIEDERMAN, W. G. 1967 Stability of turbulent channel flow, with application to Malkus's theory. *J. Fluid Mech.* **27**, 253–272.

ROBINSON, S. K. 1991 Coherent motions in the turbulent boundary-layer. *Annu. Rev. Fluid Mech.* **23**, 601–639.

SCHOPPA, W. & HUSSAIN, F. 2002 Coherent structure generation in near-wall turbulence. *J. Fluid Mech.* **453**, 57–108.

SHARMA, A. S. & MCKEON, B. J. 2013 On coherent structure in wall turbulence. *J. Fluid Mech.* **728**, 196–238.

SMITS, A. J., MCKEON, B. J. & MARUSIC, I. 2011 High–Reynolds number wall turbulence. *Annu. Rev. Fluid Mech.* **43**, 353–375.

TOMIYAMA, N. & FUKAGATA, K. 2013 Direct numerical simulation of drag reduction in a turbulent channel flow using spanwise traveling wave-like wall deformation. *Phys. Fluids* **25**, 105115.

WALEFFE, F. 1997 On a self-sustaining process in shear flows. *Phys. Fluids* **9**, 883–900.

WALSH, M. J. & WEINSTEIN, L. M. 1979 Drag and heat-transfer characteristics of small longitudinally ribbed surfaces. *AIAA J.* **17**, 770–771.

WEIDEMAN, J. A. & REDDY, S. C. 2000 A matlab differentiation matrix suite. *ACM Trans. Math. Softw.* **26**, 465–519.

YOSHINO, T., SUZUKI, Y. & KASAGI, N. 2008 Drag reduction of turbulence air channel flow with distributed micro sensors and actuators. *J. Fluid Sci. Technol.* **3**, 137–148.